**The Thesis Committee for Benjamin Michael Goldsberry**
**Certifies that this is the approved version of the following thesis:**

# Modeling Three-dimensional Acoustic Propagation in Underwater Waveguides using the Longitudinally Invariant Finite Element Method

APPROVED BY

SUPERVISING COMMITTEE:

Mark F. Hamilton, Supervisor

Marcia J. Isakson, Co-Supervisor

# Modeling Three-dimensional Acoustic Propagation in Underwater Waveguides using the Longitudinally Invariant Finite Element Method

**by**

**Benjamin Michael Goldsberry, B.A.**

**THESIS**

Presented to the Faculty of the Graduate School of

The University of Texas at Austin

in Partial Fulfillment

of the Requirements

for the Degree of

**MASTER OF SCIENCE IN ENGINEERING**

THE UNIVERSITY OF TEXAS AT AUSTIN

August 2014

In loving memory of Evelyn Botts Wester (1916-2013)

# Acknowledgments

I wish to thank the people who helped and gave me support as I completed this work. First of all, I would like to thank my family for their constant support, encouragement, and love. I would also like to thank Nathalia Basso for her inspiration, guidance, and being a wonderful best friend. Much appreciation to my friends, the Four Pack (Anthony Bonomo, Stephanie "Trinity" Konarski, and Justin "The Everyman" Gorhum). Many thanks to Dr. Mark Sussman at Florida State University and Dr. Jeffrey Housman at NASA Ames Research Center for being excellent mentors that put me on the path towards studying acoustics. Finally, I would like to thank Dr. Marcia Isakson for advising me throughout my time studying, Dr. Mark Hamilton for his extraordinary lectures on acoustics, Texas Advanced Computing Center (TACC) for their computational resources, and the Office of Naval Research, Ocean Acoustics for their financial support.

# Modeling Three-dimensional Acoustic Propagation in Underwater Waveguides using the Longitudinally Invariant Finite Element Method

Benjamin Michael Goldsberry, M.S.E
The University of Texas at Austin, 2014

Supervisors: Mark F. Hamilton
Marcia J. Isakson

Three-dimensional acoustic propagation in shallow water waveguides is studied using the longitudinally invariant finite element method. This technique is appropriate for environments with lateral variations that occur in only one dimension. In this method, a transform is applied to the three-dimensional Helmholtz equation to remove the range-independent dimension. The finite element method is employed to solve the transformed Helmholtz equation for each out-of-plane wavenumber. Finally, the inverse transform is used to transform the pressure field back to three-dimensional spatial coordinates. Due to the oscillatory nature of the inverse transform, two integration techniques are developed. The first is a Riemann sum combined with a wavenumber sampling method that efficiently captures the essential components of the integrand. The other is a modified adaptive Clenshaw-Curtis quadrature. Three-dimensional transmission loss is computed for a Pekeris

waveguide, underwater wedge, and Gaussian canyon. For each waveguide, the two integration schemes are compared in terms of accuracy and efficiency.

# Table of Contents

**Acknowledgments** v

**Abstract** vi

**List of Tables** x

**List of Figures** xi

**Chapter 1. Introduction** 1

**Chapter 2. Literature Review** 5

2.1 Existing analytical and numerical solutions to range-dependent environments . . . 6

2.2 Experiments . . . 14

**Chapter 3. Finite Element Method** 17

3.1 Problem Statement . . . 18

3.2 Cosine Transform . . . 25

3.3 Weak Form . . . 26

3.4 Discretization . . . 29

3.5 Perfectly Matched Layers . . . 31

**Chapter 4. Inverse Cosine Transform** 33

4.1 Integrand Properties . . . 34

4.2 Variable $k_y$ Integration . . . 38

4.3 Modified Adaptive Clenshaw-Curtis Quadrature . . . 40

4.3.1 Error analysis . . . 45

4.3.2 Modified Adaptive Clenshaw-Curtis Quadrature Applied to the Inverse Cosine Transform . . . 50

4.3.3 Considerations . . . 52

**Chapter 5. Results** **55**
5.1 Pekeris Waveguide . . . . . 56
5.2 ASA Wedge . . . . . 60
5.3 Gaussian Canyon . . . . . 66

**Chapter 6. Conclusion** **73**

**Appendices** **77**

**Appendix A. Modified Adaptive Clenshaw-Curtis Quadrature Algorithm** **78**

**Bibliography** **83**

**Vita** **94**

# List of Tables

3.1 Water and sediment properties for each geometry . . . . . 19

# List of Figures


3.1 (a) Physical depiction of Pekeris waveguide. (b) Computational domain of Pekeris waveguide. . . . . 21

3.2 (a) 3-D ASA wedge geometry. The bisecting plane denotes the source plane and is shown in (b). . . . . 22

3.3 (a) 3-D Gaussian canyon geometry. (b) the vertical source plane. 23

4.1 (a) Real part of the Green's function for $k_y < k$, representing propagating wave solutions. (b) Real part of the Green's function for $k_y > k$, representing evanescent wave solutions. . . 35

4.2 Real part of the Green's function for several range values. . . . 36

4.3 Variable $k_y$ spacing based on the gamma CDF function versus a constant $k_y$ spacing for 300 wavenumber values. . . . . 39

4.4 Comparison of the analytical solution to a point source in free space to the solution of Eq. (4.2) for a variable and constant $k_y$ spacing. Note that the variable $k_y$ spacing is more accurate than the constant spacing. . . . . 40

5.1 Comparison of the variable $k_y$ method, modified adaptive Clenshaw-Curtis quadrature (MACC), and the wavenumber integration code OASES in the source plane ($y = 0$) at a depth of (a) 24 m, (b) 98 m. . . . . 57

5.2 Comparison of the variable $k_y$ method, modified adaptive Clenshaw-Curtis quadrature (MACC), and the wavenumber integration code OASES along the invariant coordinate $y$ at a depth of 89 m. 58

5.3 Modified adaptive Clenshaw-Curtis quadrature (MACC) compared with the wavenumber integration code OASES along the invariant coordinate $y$ at a depth of 89 m. . . . . 59

5.4 Longitudinally invariant finite element method (LIFEM) versus the axi-symmetric parabolic equation code RAM in the source plane ($y = 0$) at a depth of (a) 30 m, and (b) 100 m. . . . . 62

5.5 Source plane transmission loss computed using the variable $k_y$ method. . . . . 63

5.6 "Top down" view of the ASA wedge at a depth of (a) 30 m, and (b) 100 m. . . . . 64

5.7 Comparison of the variable $k_y$ and modified adaptive Clenshaw-Curtis quadrature (MACC) for the ASA wedge along the invariant coordinate $y$ at $x = 0$, and at a depth of (a) 30 m, and (b) 150 m. . . . . 65

5.8 Source plane solution to the Gaussian canyon using the variable $k_y$ method. . . . . 67

5.9 "Top down" view of the Gaussian canyon at a depth of (a) 10 m, (b) 35 m, (c) 100 m, (d) 150 m, and (e) 180 m. . . . . 69

5.10 Comparison of modified adaptive Clenshaw-Curtis quadrature (MACC) and the variable $k_y$ method for the Gaussian canyon in the source plane ($y = 0$), and at a depth of (a) 35 m, and (b) 130 m. . . . . 70

5.11 Comparison of the variable $k_y$ and modified adaptive Clenshaw-Curtis quadrature (MACC) for the Gaussian canyon along the $y$ coordinate at the source location ($x = 5000$ m), and at a depth of (a) 30 m, and (b) 35 m. . . . . 71

5.12 Comparison of the variable $k_y$ and modified adaptive Clenshaw-Curtis quadrature (MACC) for the Gaussian canyon along the $y$ coordinate at a depth of 35 m and (a) 1000 m from the source ($x = 6000$ m), and (b) 2000 m from the source ($x = 7000$ m). . 72

A.1 (a) Comparison of Chebyshev, Lagrange, and linear interpolation with the exact function for the interval 0 to $k_c/2$. (b) Percent error for Chebyshev, Lagrange, and linear interpolation. (c) Magnitude of the Chebyshev coefficients. . . . . 81

A.2 (a) Comparison of Chebyshev, Lagrange, and linear interpolation with the exact function for the interval $k_c/2$ to $k_c$. (a) Magnitude of the Chebyshev coefficients. . . . . 82

# Chapter 1

# Introduction

Acoustic propagation in shallow water environments presents a wealth of physics not found in the deep sea. In shallow water environments, sound interacts with both the sea surface and the ocean bottom. Because of this, the sediment composition, layer structure, and bathymetry all play an important factor in acoustic propagation. These effects have a drastic impact on the transmission loss in the sonar equation, which influences the effective range of a sonar or underwater communications system. For this reason, the impact of the sediment properties and bathymetry on the transmission loss of a shallow water waveguide must be investigated.

An area of great study is the effect of the bathymetry in a three-dimensional region of the ocean on the transmission loss of a sonar [1]. These types of environments are known as range-dependent waveguides. They exhibit acoustic phenomena not seen in range-independent waveguides, where the bottom bathymetry does not change. The most prevalent phenomenon due range-dependent bathymetry is horizontal refraction. When sound propagates from deep water to shallow water, the repeated specular reflections between the air-water interface and the sloping ocean bottom will cause the acoustic

energy to refract down towards deeper water. Weston in [2] mathematically showed the existence of horizontal refraction in underwater waveguides using ray acoustics and proved that the effect is only due to the sloping bathymetry of a range-dependent waveguide. Though horizontal refraction was understood in the 1960's and 1970's, it was not experimentally observed in the ocean until 1988, when Doolittle and Tolstoy obtained experimental measurements of horizontal refraction along the East Australian Continental Slope [3]. Because ocean experiments are costly and difficult to perform, this effect must be investigated with mathematical models. However, it is difficult to provide analytical solutions to the acoustic pressure field for range-dependent environments. Therefore, numerical methods are used. A profusion of literature exists in deriving and implementing normal modes, rays, virtual source, and parabolic equation methods to range-dependent environments, which are discussed in the next chapter. However, each of these models have assumptions to the governing physics, including a slowly-varying bathymetry [1].

This work employs the finite element method to model three-dimensional range-dependent ocean waveguides. Unlike the previously mentioned models, the finite element method solves the governing equations exactly; there are no assumptions to the physics. In addition, sediment layers and sound speed profiles can be easily and accurately incorporated. However, three-dimensional finite element methods are computationally demanding. If the bathymetry of a waveguide does not vary along one Cartesian spatial coordinate, mathematical techniques can be applied to reduce the dimensionality of the problem and

make the numerical computations tractable. Therefore, a longitudinally invariant finite element model is proposed, where a Fourier transform is applied to the invariant direction. Then, three-dimensional acoustic pressure fields can be solved by computing multiple two-dimensional finite element models for different out-of-plane wavenumbers and applying the inverse Fourier transform. However, due to the oscillatory nature of the inverse transform integrand, an efficient integration scheme needs to be developed.

This thesis attempts to answer the following questions:

1. **How accurate is the longitudinally invariant finite element method in computing the transmission loss in a three-dimensional range-dependent waveguide?**

2. **What is an efficient integration scheme that uses the least number of finite element evaluations and calculates the inverse transform accurately?**

The first question is addressed by investigating three different underwater environments. To ensure that the longitudinally invariant finite element model is derived and implemented correctly, a range-independent environment is first investigated. Then the introduction of range-dependence in the finite element model is assessed by computing the transmission loss in a simple underwater acoustic wedge environment. Finally, an underwater Gaussian canyon environment is investigated as a proof of concept.

To address the second question, two integration schemes are developed. The first is a discretization of the integral into a Riemann sum, but the abscissa are allowed to have variable spacing to efficiently compute the integral. The second scheme is a modified adaptive Clenshaw-Curtis quadrature. For each waveguide, both integration schemes are compared and contrasted in terms of accuracy in computing a three-dimensional acoustic pressure field, and the number of finite element evaluations.

# Chapter 2

# Literature Review

Over the past several decades, many analytical and numerical solutions have been developed to approximate the wave equation in range-dependent shallow water waveguides. In addition, there have been numerous tank and ocean experiments verifying three-dimensional effects created by range-dependent bathymetry, the most notable being horizontal refraction. Early work dealt with finding solutions to the wave equation in an underwater wedge with a constant slope that is infinite in extent parallel to the wedge apex, with the air-water interface and bottom interface approximated as a pressure-release boundary condition and a rigid boundary condition, respectively. Currently, most modern models have the ability to model an arbitrary bathymetry profile, as long as the profile lies within the approximations of the given numerical model. The aim of this chapter is to examine previous work on deriving analytical and numerical solutions to range-dependent environments. The first section discusses relevant analytical and numerical models. The last section discusses the relevant experiments performed.

## 2.1 Existing analytical and numerical solutions to range-dependent environments

In 1959 and 1960, D.E. Weston wrote two papers concerning acoustic propagation in a shallow-water waveguide where the bottom boundary height varies with horizontal range [2, 4]. In the second paper, Weston focuses on the effect of sound propagation in a three-dimensional medium in which the bottom boundary is allowed to slowly vary with horizontal range. A consequence of sound propagation in a three-dimensional medium with a sloping bottom is the existence of the phenomenon known as "horizontal refraction." This phenomenon occurs when repeated bottom and surface specular reflections of a sound wave traversing a path oblique to the slope apex produces a curvature of the horizontal path of the wave. Weston's paper shows the existence of horizontal refraction by considering simple ray propagation up a perfectly reflecting inclined wedge with a constant sound speed profile in the water column. When a ray is launched at a horizontal angle oblique to the wedge apex, repeated specular reflections from the sloped surface causes the ray to refract back towards deeper water, creating a hyperbolic path shape in the horizontal plane.

In 1964, Allan D. Pierce in [5] generalized normal mode theory of sound propagation in a perfectly stratified medium to an "almost-stratified medium," which is a medium whose properties and boundaries are allowed to gradually vary with horizontal distances. A solution to the theory is obtained by making an adiabatic assumption, meaning modes propagate independently and do not

transfer energy to another mode. This theory is also referred to as uncoupled normal modes. In a medium where the horizontal changes are small, this assumption is valid, and, as the slope of the bottom approaches zero (meaning the bottom is perfectly flat), the solution is exact. When applied to an underwater wedge environment with a constant slope, the results show that the modes travel a hyperbolic path along the wedge, which is consistent with Weston's results in [2]. Pierce also notes that, for a given frequency, if a receiver lies on the parabolic path the acoustic energy arrives at the receiver at two distinct times. The first arrival is the direct arrival from the source to receiver, while the second arrival is the horizontally refracted sound due to the wedge. In addition, the solution shows that there exists shadow regions, where there are no horizontal ray paths connecting source and receiver. It is also important to note that, in general, different frequencies arriving at different times do not travel on the same horizontal path.

In [6], Graves et al. apply Pierce's adiabatic uncoupled modes to an underwater wedge environment which is invariant parallel to the apex. A Fourier transform is applied to the invariant coordinate to obtain an exact solution to the uncoupled mode equations. The accuracy of the adiabatic assumption is addressed through comparison with the exact solution of an underwater wedge with a small, constant slope and constant sound speed. Small discrepancies between the adiabatic assumption and the exact solution were found in the intensity near the mode cut-off depth and in higher order modes. The authors note that the mode coupling terms should reduce the

discrepancies between normal modes and the exact solution, and inclusion of the coupling terms will allow normal modes to be applied to more rapid environmental changes. In addition, for long range propagation, energy from higher modes will be transferred to lower modes before the former arrives at its cut-off point. Since the adiabatic mode formulation does not allow for modes to redistribute energy, the adiabatic solution will under-predict the intensity.

Solutions to coupled mode theory, where the mode coupling terms are not neglected, were also sought so that environments with less gradual slope variations can be considered. In [7], Rutherford and Hawker show that the rigid bottom boundary condition used by Pierce in [5] is approximate, and when surfaces are allowed to vary more rapidly, the physically realistic conservation of particle velocity normal to the boundary must be used instead of the conservation of particle velocity with respect to the vertical coordinate. Using the approximate boundary condition of conservation of particle velocity in the vertical coordinate leads to nonconservation of energy in coupled mode theory. The authors re-derive coupled mode theory using the physical boundary conditions of continuity of normal particle velocity, and terms which conserve energy to first order in the slopes of the horizontal boundary are retained.

Ray theory methods were also developed to study refraction effects in underwater wedge environments. In 1973, ray theory was generalized to model geometries with weak range dependence by Weinberg and Burridge in [8]. Following in the same manner as Pierce, the eikonal and transport equations, which are used to calculate the phase and amplitudes of acoustic

rays, are generalized to propagation in an "almost-stratified medium." In [9], Harrison analyzes the overlap between ray theory and normal modes to study shadow regions in an underwater wedge environment. At low frequencies, the launch angles of the rays must be restricted to discrete values corresponding to the angles given by the phase speeds of propagating modes. This restriction causes the rays to trace out the path of the modes, creating shadow zones. Harrison also notes that interference patterns found along the wedge is caused by the interference resulting from the many possible horizontal paths of a single mode. In [10], Westwood provides a broadband model of the three-dimensional penetrable wedge by extending two-dimensional complex eigenray theory to three dimensions. Broadband field computations are achieved by interpolating the eigenray characteristics between frequencies.

Normal mode theory describing underwater wedge environments with a penetrable fluid bottom was also developed. The Helmholtz equation becomes non-separable when dealing with penetrable fluid bottoms with a variable bottom profile. Even if the boundary surfaces are matched by a separable coordinate system, the boundary conditions on a fluid-fluid interface ensure that the Helmholtz equation is not separable. In [11], Evans treats the wedge as a number of stepwise, range-independent Pekeris waveguides. Backscatter is included by conserving energy between each range-independent step. In [12], Arnold and Fensen investigate the transition region of both uncoupled normal modes and rays, where initially trapped energy in a waveguide penetrates into the bottom medium. The authors show that uncoupled normal modes and ray

theory provide a good approximation with weak range-dependence; however, this cannot be applied to the more general problem of acoustic propagation in any wedge environment with bottom penetration. For upslope propagation, rays that start as initially totally internally reflected eventually penetrate into the bottom. Similarly, trapped modes propagating upslope approach cut-off and transition to a leaky mode. Lack of knowledge of the transition between trapped and leaky modes has prevented existing ray and normal mode models to effectively describe upslope propagation. The authors state that the present theories do not provide any insight on whether the transition requires intermodal coupling or whether a mode retains its separate identity in the transition from a trapped mode to a leaky mode. The authors address this problem by deriving an integral equation which describes the transition behavior as a mode approaches cut-off. The transition function obtained is similar to Pierce's investigation of the disappearance of trapped modes as they approach cut-off in [13], where an analytical solution of a parabolic equation describing upslope propagation of an initially trapped mode is derived.

In [14], Buckingham derives an analytical solution to a penetrable wedge. The dispersion relation in a wedge environment suggests that a coordinate transformation to an "effective" wedge, with the apex displaced and the bottom replaced with a pressure-release boundary condition, considerably reduces the complexity of the penetrable wedge problem while still being exact. This "effective" wedge removes the range dependence of the modal functions, making the Helmholtz equation separable, and provides an exact solution to

a wedge environment with a penetrable fluid bottom.

In [15], Arnold and Fensen seek a more suitable generalization of mode theory of propagation in a wedge environment, called "intrinsic" modes, where an intrinsic mode is not coupled to another intrinsic mode, and each intrinsic mode contains the contribution of normal coupled local modes. The authors show that the zeroth order approximation to the intrinsic modes is equivalent to the adiabatic modes derived by Pierce in [5], with the addition of the transition function from trapped to leaky modes. The next order of approximation of the intrinsic modes give the local coupled normal modes and coupling coefficients. Using a perturbation method, Desaubies and Dysthe in [16] develop a theory of intrinsic normal modes in a general range-dependent waveguide with a penetrable fluid bottom.

The parabolic equation method (PE) has also been used to study wave propagation in a medium with variable bathymetry. PE was first applied to underwater acoustics in 1973 by Hardin and Tappert [17]. In 1977, Tappert published lecture notes fully describing PE theory with application to underwater acoustics [18]. The derivation of PE carries three major assumptions: the receiver is in the far-field, the sound speed and bathymetry vary weakly in range, and backscattering is negligible [19]. These assumptions allow the Helmholtz equation, which is a second order elliptic equation, to be approximated by a first order parabolic equation by removing the second derivative in range, such that numerical solutions can be calculated using marching techniques in range. In [20], McDaniel investigates the consequences of ap-

proximating the Helmholtz equation with a parabolic equation by comparing the PE equation solution to a coupled mode solution. McDaniel finds that the paraxial assumption (neglecting the second derivative in range to reduce the order of the Helmholtz equation) introduces increasing phase errors for wide propagation angles. However, for on-axis and low angle propagation, the PE equation provides a reasonable solution. PE also contains a square root pseudo-differential operator, which must be expanded by polynomials or rational functions such that the phase errors are minimized over a wide range of propagation angles. The square root operator is expanded by Tappert in [18] and Claerbout in [21]; however, both of these expansions have increasing phase error with increasing angle. A high angle expansion is developed by Greene in [22], which minimizes phase errors over an angle interval of 0-40 degrees. In [23], Halpern and Trefethen find that a Padé series expansion does not minimize the errors for all angles of choice but provides the highest accuracy in the main propagation direction. In [24], Bamberger et al. derive a new family of higher order PE approximations based on the Padé series expansion. Collins in [25] applies the high order wide angle PE in [24] to underwater propagation. These high order equations can be solved by either finite-difference or finite element techniques.

Three-dimensional PE models have also been created. A wide angle PE model adapted to study ocean bottoms with range dependence is the FOR3D, created by Lee et al. in [26]. However, fully three-dimensional PE models are inefficient for long range computations. Therefore, hybrid models have been

developed. Collins develops an adiabatic mode PE to efficiently calculate long range acoustic propagation in [27]. A far-field wave equation is derived, and the pressure field is expressed in terms of uncoupled propagating modes. The modal amplitudes are then solved using a two-dimensional PE model. In [28], Abawi et al. derive a coupled mode PE model, which is a generalization of the adiabatic PE created by Collins in [27]. This model is energy conserving, and involves both mode and azimuthal coupling.

Application of PE to upslope and downslope propagation in an underwater wedge have been used to display the accuracy of PE for underwater acoustic propagation. In [29], Jensen and Kuperman use PE to study mode cut-off behavior as modes propagate upslope. The authors show that as the mode approaches the cut-off depth, the angles of the modes transition from being below the grazing critical angle of the sediment (corresponding to trapped modes) to being above the grazing critical angle of the sediment, causing the mode to penetrate into the bottom. This environment leads to the modal energy radiating into the bottom as a well-defined beam.

In 1995, the Acoustical Society of America created the "ASA wedge benchmark," where several wedge problems were studied using a plethora of models. Approximate analytical solutions were derived by Deane and Buckingham [30], an adiabatic normal mode approach was used by Tindle and Zhang [31], and a new theory incorporating image sources that can include fluid and elastic wedge bottoms was derived by Deane and Buckingham in [32]. In [33], Jensen et al. supply a coupled mode solution and two PE models, showing that

the coupled mode solution is the most able to provide benchmark solutions. PE models that describe broadband pulse propagation in a wedge environment are derived by Sturm in [34].

## 2.2 Experiments

In 1960, an experiment was conducted where sound created by explosive charges from Perth, Australia propagated to a hydrophone array at Bermuda. The data recorded contained two arrivals of the acoustic energy. Using an adiabatic mode model, which includes horizontal refraction, Heaney et al. in [35] show that the double pulse arrival is due to the presence of horizontal refraction. The authors claim that the initial arrival follows a propagation path that lies just south of Africa, while the horizontally refracted path follows a longer path to the south and comes close to the coast of Brazil.

Doolittle et al. in 1988 performed an acoustic transmission experiment in the East Australian Continental Slope [3]. The experiment was conducted with two ships, one with a towed source and the other with an array of hydrophones starting in water approximately 500 m deep with an initial separation of 34 km. The angle of arrival for the acoustic energy was calculated by beamforming the signals received at the hydrophones. There were measured angle of arrivals at approximately 88 degrees, nearly broadside to the array, showing evidence of horizontal refraction.

Horizontal refraction was measured off the east coast of Florida in 2007 by Heaney and Murray [36]. Continuous wave tones were generated by a towed

source and recorded on a horizontal line array, with the separation ranging from 10 to 80 km. Multiple horizontal arrivals, with angle of arrivals up to 30 degrees, were observed. When the source was beyond 20 km, the acoustic energy from the refracted path dominated the energy from the direct path. Horizontal focusing was also noted for source to receiver distances of 40 to 80 km. In [37], Ballard models this experiment using a hybrid adiabatic mode model, where the modal amplitude equations are solved using PE.

In 2010, an undersea volcano 8 km southeast of Sarigan Island erupted, emitting low-frequency acoustic energy with broadband spikes. The acoustic energy emitted from this eruption was recorded on a pair of hydrophone arrays 2250 km from Sarigan Island by Heaney et al. in [38]. An adiabatic mode PE model was used to model the eruption. The model predicted horizontal refraction, scattering from Sarigan Island, and diffraction, which agreed with the recorded experimental observations.

Several tank experiments have been conducted to verify three-dimensional mode propagation in underwater wedge environments. The adiabatic approximation was validated by Eby et al. in [39] for propagation with wedge slopes of around 1 degree in a small tank experiment. Ingenito and Wolf in [40] validate the adiabatic approximation for downslope propagation in the ocean for slopes of 0.3-0.9 degrees. Experiments conducted by Tindle, Hobaek, and Muir described in [41] show that it is possible to generate uncoupled modes in a wedge using a curved array source that follows an arc of a circle centered on the wedge apex. However, if the line source is vertical, the generated modes are

coupled and the sound field exhibits structure due to mode interference. In addition, the phenomena of mode capture, which is the gradual appearance of a trapped mode down-range when the water depth at the source cannot support the mode, is theoretically predicted and experimentally verified by Tindle and Deane in [42]. This phenomenon is a product of the fact that the total number of modes in a wedge waveguide is the discrete sum of trapped modes in addition to the integral of continuous modes. However, as the water depth increases down-slope, the number of discrete modes that can propagate increase, and the energy associated with a continuous mode is transferred into a trapped mode when the water depth is adequate to support that mode. The PE model by Jensen and Tindle in [43] accurately describe the results of this experiment.

# Chapter 3

# Finite Element Method

The finite element method (FEM) is a numerical technique for providing approximate solutions to boundary-value problems. The solution of the governing partial differential equation (PDE) is sought using variational methods, in which the PDE is represented in a weak form. The weak form is an integral statement of a PDE in which differentiation of a dependent variable is transferred to a weight function such that all natural boundary conditions are included in the integral statement [44]. Numerical solutions to the integral statement are found by subdividing the domain of the PDE into simple subdomains, or finite elements. The dependent variables are then approximated by an expansion into a basis set in each subdomain. The coefficients of the basis set functions can then be solved for numerically. As the size of each element decreases to zero, the approximate solution converges to the unique solution of the governing PDE which satisfies the given boundary conditions [45]. This method has been adapted to many problems in engineering and physics, and a full derivation of this method can be found in [44–46]. FEM has been successfully applied to many interior and exterior acoustics problems, including underwater scattering problems in [47]. FEM is used to study transmission loss and reverberation from a rough seabed in a shallow water waveguide in

[48]. Two-dimensional FEM is used to study acoustic propagation near the southern and western Australian continental shelf in [49]. However, little work has been done in applying FEM to long range 3-D shallow-water acoustic propagation. This is due to the fact that many elements are needed to accurately model a long range waveguide. However, if the geometry of the domain only has lateral variations in one spatial coordinate, a transform can be applied to remove the range-independent dimension. A 2-D FEM algorithm can then be used to solve the transformed Helmholtz equation for each out-of-plane wavenumber. The inverse transform is then applied to the 2-D computations to produce an acoustic pressure field in 3-D spatial coordinates.

In the first section of this chapter, the problem geometries, along with the corresponding PDEs governing the acoustic pressure field are described. In the second section, the cosine transform is applied to the governing equations. In the third section, the weak form is derived. In the fourth section, the weak form is discretized and approximated such that solutions can be found numerically. In the fifth section, perfectly matched layers are discussed.

## 3.1 Problem Statement

Three geometries will be considered in this work. The first is a flat, range-independent ocean bottom environment (also known as a Pekeris waveguide). A physical depiction and the finite element computational domain of the Pekeris waveguide is shown in Fig. 3.1. Since the computational domain must be finite, perfectly matched layers (PML) are used to truncate the domain.

Table 3.1: Water and sediment properties for each geometry

| **Geometry** | $\rho_1$ (kg/m$^3$) | $c_1$ (m/s) | $\rho_2$ (kg/m$^3$) | $c_2$ (m/s) | $a$ (dB/$\lambda$) | $z_s$ (m) |
|---|---|---|---|---|---|---|
| Flat | 1000 | 1500 | 1500 | 1700 | 0.5 | 25 |
| Wedge | 1000 | 1500 | 1500 | 1700 | 0.5 | 100 |
| Canyon | 1000 | 1500 | 1500 | 1700 | 0.1 | 30 |

These layers are discussed further in Sec. 3.5. The water column depth is 100 m, and the source depth is 25 m. The second geometry considered is the "ASA Wedge," a simple underwater wedge environment [33]. The three-dimensional geometry is shown in Fig. 3.2a and the vertical cut-plane where the source is located is shown in Fig. 3.2b. The wedge angle is 2.86°, and the water depth is 200 m at the source location. The source is located 4000 m away from the wedge apex. The third geometry is a Gaussian-shaped underwater canyon, modeled after [1] and shown in Fig. 3.3a, with a vertical cut plane shown in Fig. 3.3b. The ocean bottom depth, $z(x)$, is described by

$$z\left(x\right) = -200 - 500 \exp\left[-(x-5)^2/4\right], \tag{3.1}$$

where $x$ is the cross-range coordinate in kilometers.

For all three geometries, a Cartesian coordinate system is used and defined such that the source is located at $(0, 0, z_s)$. In addition, the bottom profile is invariant, or range independent, along the one spatial Cartesian coordinate. This invariant coordinate will be chosen as the $y$ coordinate; $z$ will be the depth coordinate and $x$ will be the horizontal coordinate.

Table 3.1 show the water and sediment parameters for each geometry, where $\rho_{1,2}$ and $c_{1,2}$ are the water and sediment density and sound speed, re-

spectively, $a$ is the attenuation in the sediment, and $z_s$ is the source depth. In all three models, the sediment parameters are chosen to be similar to that of sand. Because the acoustic wavelengths under consideration are large compared to the sediment grain size and it is assumed that the sandy sediments exhibit low shear coupling, the sediment can be adequately modeled as a continuous fluid. Chapter 8 of [50] discusses the accuracy of modeling sediments as a fluid.

For a time-harmonic point source located in the water domain, the acoustic pressure field in the water and sediment is governed by the following pair of three-dimensional Helmholtz equations, boundary conditions, and interface conditions between the water column and the sediment:

$$\rho_1 \nabla \cdot \left( \frac{1}{\rho_1} \nabla p_1(\mathbf{x}) \right) + k_1^2 p_1(\mathbf{x}) = -Q(\omega)\delta(\mathbf{x} - \mathbf{x}_s), \quad \mathbf{x} \in \Omega_1 \tag{3.2}$$

$$\rho_2 \nabla \cdot \left( \frac{1}{\rho_2} \nabla p_2(\mathbf{x}) \right) + k_2^2 p_2(\mathbf{x}) = 0, \quad \mathbf{x} \in \Omega_2 \tag{3.3}$$

$$p_1(\mathbf{x}) = 0, \quad \mathbf{x} \in \partial\Omega_1 \tag{3.4}$$

$$p_1(\mathbf{x}) = p_2(\mathbf{x}), \quad \mathbf{x} \in \partial\Omega_2 \tag{3.5}$$

$$\frac{1}{\rho_1} \frac{\partial p_1(\mathbf{x})}{\partial n} = \frac{1}{\rho_2} \frac{\partial p_2(\mathbf{x})}{\partial n}, \quad \mathbf{x} \in \partial\Omega_2 \tag{3.6}$$

where $\mathbf{x}$ is the Cartesian coordinate $(x, y, z)$, $\nabla = \begin{bmatrix} \frac{\partial}{\partial x} & \frac{\partial}{\partial y} & \frac{\partial}{\partial z} \end{bmatrix}^T$, $p_1$ and $p_2$ are the acoustic pressures in the water and sediment, respectively, $\mathbf{x}_s$ is the source location, $\Omega_1$ and $\Omega_2$ denote the water and sediment domains, respectively, $\partial\Omega_1$ is the air-water interface, and $\partial\Omega_2$ is the fluid-sediment interface. The wavenumbers $k_1$ and $k_2$ are defined as $\omega/c_1(\mathbf{x})$ and $\omega/c_2(\mathbf{x})$, where $c_1(\mathbf{x})$ and $c_2(\mathbf{x})$ are the phase sound speed profiles for the water and sediment domain,

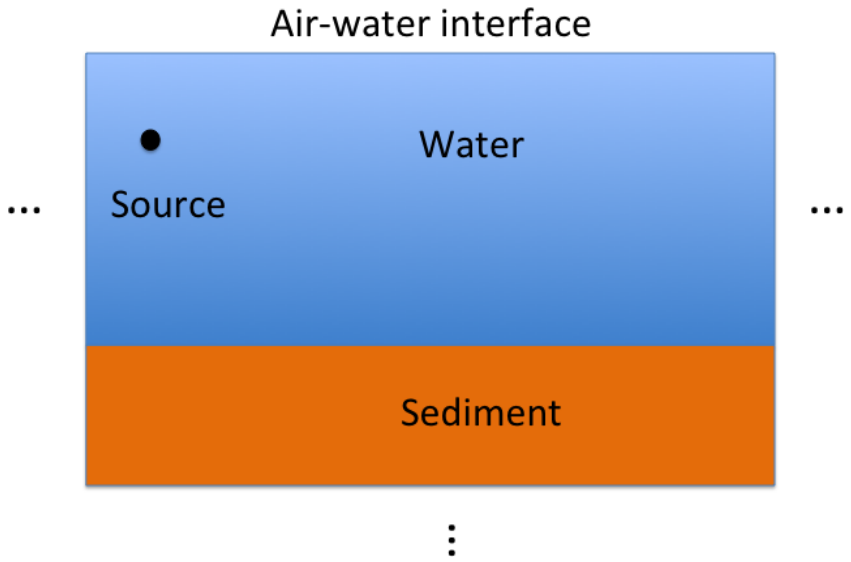


(a)

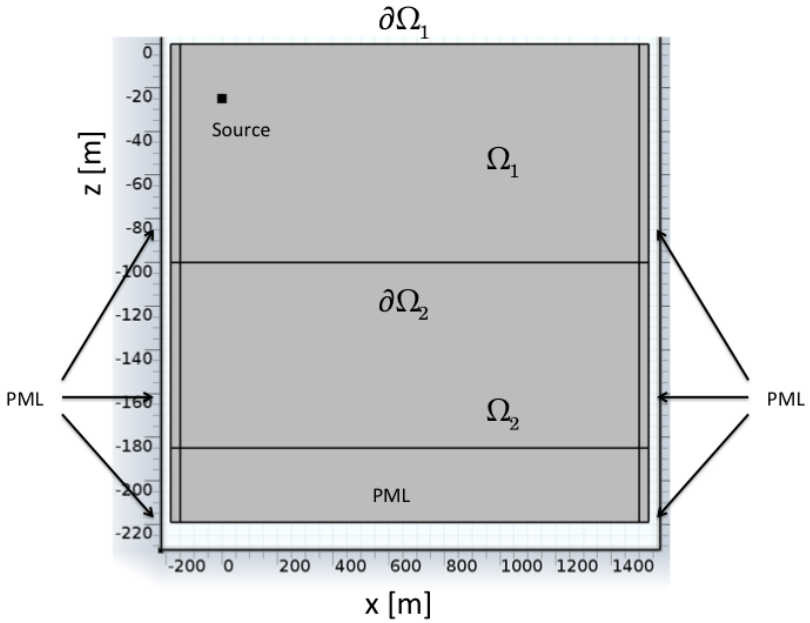


(b)

Figure 3.1: (a) Physical depiction of Pekeris waveguide. (b) Computational domain of Pekeris waveguide.

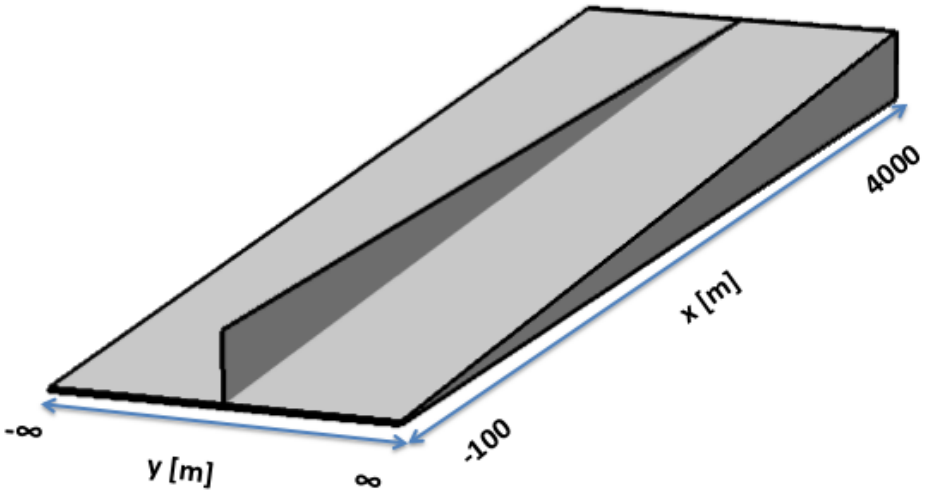


(a)

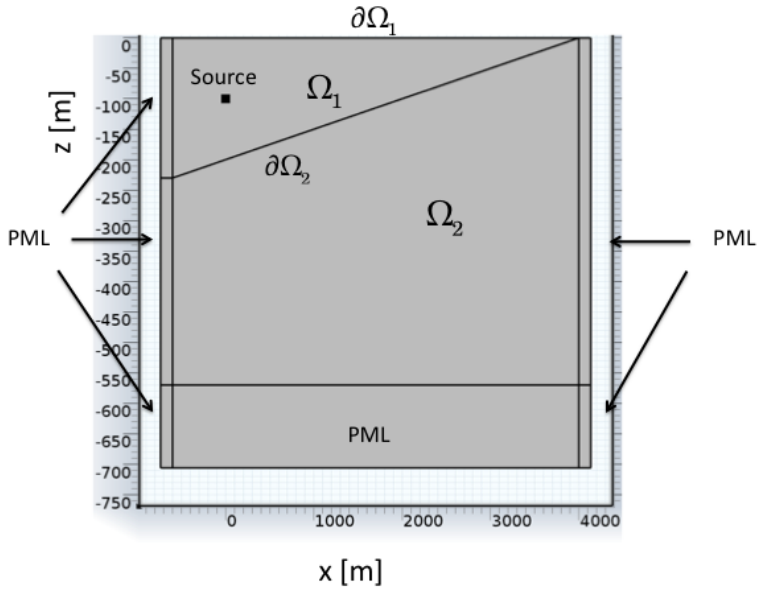


(b)

Figure 3.2: (a) 3-D ASA wedge geometry. The bisecting plane denotes the source plane and is shown in (b).

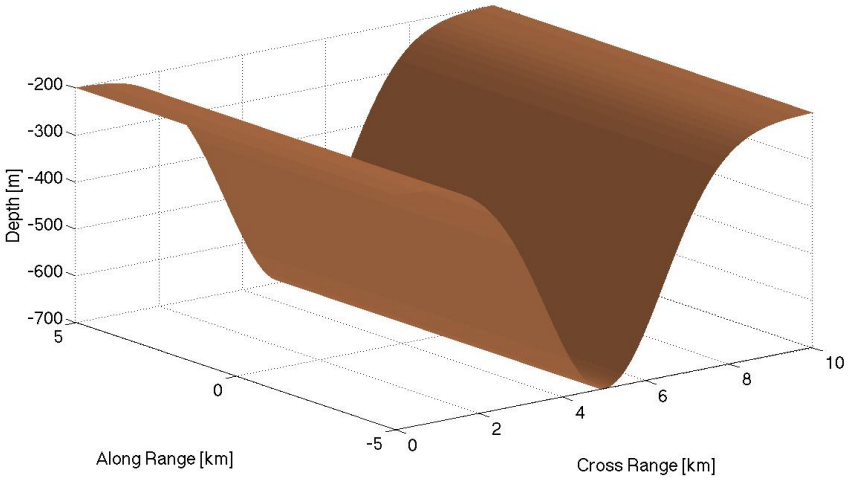


(a)

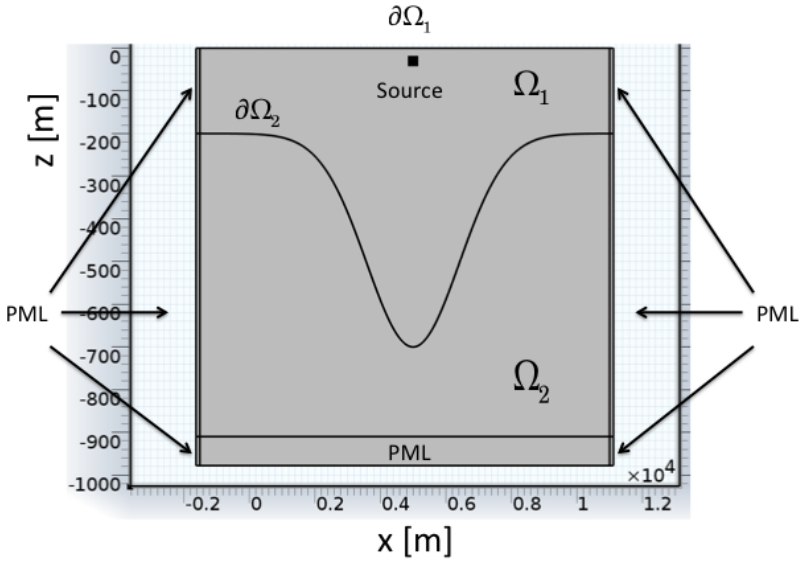


(b)

Figure 3.3: (a) 3-D Gaussian canyon geometry. (b) the vertical source plane.

and $\omega$ is the angular frequency, $2\pi f$, where $f$ is the frequency. Equation (3.5) ensures the continuity of pressure across the interface, and Eq. (3.6) ensures the continuity of normal particle velocity. The source strength $Q(\omega)$ is defined as the source amplitude of a particular frequency component. This quantity is determined by requiring that the acoustic pressure produced by a point source at the computed frequency is 1 $\mu$Pa at a distance of 1 m in a free space environment [51]. In underwater acoustics, the sound field is usually described in terms of transmission loss, defined as

$$\mathrm{TL} = -20 \log_{10} \left| \frac{p}{p_{\mathrm{ref}}} \right|, \tag{3.7}$$

where $p_{\mathrm{ref}}$ is the pressure produced at a distance of 1 m by a point source at the computed frequency in a free space environment [19]. Due to the way the source strength is defined, $p_{\mathrm{ref}} = 1\,\mu$Pa for all transmission loss calculations.

It is important to address the fact that, in addition to the stated equations, governing equations and boundary conditions must also be derived for each perfectly matched layer subdomain. However, the governing equations within the perfectly matched layers are identical to the derivation presented for the water and the sediment domain (except for the existence of a complex Cartesian coordinate system, which will be described in Sec. 3.5). For this reason, only the governing equations and weak forms corresponding to the water, sediment, and the boundary separating these two domains will be described in this work. For each scenario under consideration, the density is constant in each fluid domain, allowing the density functions to cancel in Eqs. (3.2)

and (3.3). However, density can be kept in the finite element derivation in scenarios where density is non-constant.

It is typical in computational underwater acoustics to model the sediment as an infinite half-space. In addition, the waveguide is infinite in extent. The acoustic waves traveling towards infinity therefore should not reflect at the infinite boundaries. To ensure the well-posedness of the solution, an extra condition must be enforced:

$$\lim_{|\mathbf{r}|\to\infty} \mathbf{r}\left(\frac{\partial p_{1,2}}{\partial \mathbf{r}} - ik_{1,2}p_{1,2}\right) = 0, \tag{3.8}$$

where $\mathbf{r} = |\mathbf{x} - \mathbf{x}_s|$. This is called the Sommerfeld radiation condition, and ensures that no reflected waves arise from the boundaries at infinity [45].

## 3.2 Cosine Transform

If the source is located at the $y = 0$ plane, the geometry is invariant in the $y$ coordinate, and the sound speed is only a function of $(x, z)$, then the acoustic pressure must be an even function about the $y = 0$ plane. To remove the range-independent coordinate, a Fourier transform is applied over the $y$ coordinate ($-\infty \leq y \leq \infty$). However, since the acoustic pressure is an even function about the $y = 0$ plane, the imaginary term of the Fourier kernel cancels, and integration only needs to be performed over the positive real line. Therefore, the Fourier integral is identical to a cosine transform, resulting in

the transform pair

$$P(x, k_y, z) = \int_0^\infty p(x, y, z) \cos(k_y y)\, dy, \tag{3.9}$$

$$p(x, y, z) = \frac{2}{\pi} \int_0^\infty P(x, k_y, z) \cos(k_y y)\, dk_y. \tag{3.10}$$

Applying Eq. (3.9) to the pair of Helmholtz equations, Eqns. (3.2) and (3.3), give

$$\nabla^2 P_1(x, k_y, z) + \left(k_1^2 - k_y^2\right) P_1(x, k_y, z) = -\frac{1}{2} Q(\omega) \delta(\mathbf{x} - \mathbf{x}_s), \tag{3.11}$$

$$\nabla^2 P_2(x, k_y, z) + \left(k_2^2 - k_y^2\right) P_2(x, k_y, z) = 0, \tag{3.12}$$

where the Laplacian, $\nabla^2 = \left[\frac{\partial^2}{\partial x^2} \quad \frac{\partial^2}{\partial z^2}\right]$, is now a 2-D operator. Note that the source term in Eq. (3.11) is divided by half; this is due to the fact that the cosine transform of a Dirac delta is equal to 1/2. Eqns. (3.11) and (3.12) are then recast into a weak formulation.

## 3.3 Weak Form

The first step of the finite element method is to recast the governing PDEs into a weak formulation. Following in the steps of [46], Eqns. (3.11) and (3.12) are multiplied by a test function, $v(\mathbf{x})$, and integrated over the domain respective to each equation, yielding

$$\int_{\Omega_1} \left(\nabla^2 P_1\right) v\, d\Omega_1 + \left(k_1^2 - k_y^2\right) \int_{\Omega_1} P_1 v\, d\Omega_1 = -\frac{1}{2} Q(\omega) \int_{\Omega_1} \delta(\mathbf{x} - \mathbf{x}_s) v\, d\Omega_1, \tag{3.13}$$

$$\int_{\Omega_2} \left(\nabla^2 P_2\right) v \, d\Omega_2 + \left(k_2^2 - k_y^2\right) \int_{\Omega_2} P_2 v \, d\Omega_2 = 0. \tag{3.14}$$

Green's first identity, an application of the divergence theorem, is then applied to the first volume integrals in Eqns. (3.13) and (3.14)

$$\begin{aligned} &-\int_{\Omega_1} \nabla P_1 \cdot \nabla v \, d\Omega_1 + \left(k_1^2 - k_y^2\right) \int_{\Omega_1} P_1 v \, d\Omega_1 = \\ &-\frac{1}{2} Q(\omega) \int_{\Omega_1} \delta(\mathbf{x} - \mathbf{x}_s) v \, d\Omega_1 - \int_{\partial\Omega_1} v \left(\nabla P_1 \cdot n\right) dS - \int_{\partial\Omega_2} v \left(\nabla P_1 \cdot n\right) dS, \end{aligned} \tag{3.15}$$

$$-\int_{\Omega_2} \nabla P_2 \cdot \nabla v \, d\Omega_2 + \left(k_2^2 - k_y^2\right) \int_{\Omega_2} P_2 v \, d\Omega_2 = -\int_{\partial\Omega_2} v \left(\nabla P_2 \cdot n\right) dS, \tag{3.16}$$

where $n$ is the outward-facing normal to $\Omega_1$ in Eq. (3.15) and $\Omega_2$ in Eq. (3.16). Eqns. (3.15) and (3.16) are then added together. By multiplying Eq. (3.15) by $1/\rho_1$ and Eq. (3.16) by $1/\rho_2$ the continuity of normal particle velocity, Eq. (3.6), will cause the two surface integrals over $\partial\Omega_2$ to be equal to each other, which cancel when the two equations are added together. The sum of the two equations become

$$\begin{aligned} &-\frac{1}{\rho_1} \int_{\Omega_1} \nabla P_1 \cdot \nabla v \, d\Omega_1 - \frac{1}{\rho_2} \int_{\Omega_2} \nabla P_2 \cdot \nabla v \, d\Omega_2 + \\ &\qquad \frac{1}{\rho_1} \left(k_1^2 - k_y^2\right) \int_{\Omega_1} P_1 v \, d\Omega_1 + \frac{1}{\rho_2} \left(k_2^2 - k_y^2\right) \int_{\Omega_2} P_2 v \, d\Omega_2 = \\ &\qquad\qquad -\frac{Q(\omega)}{2\rho_1} v(\mathbf{x}_s) - \frac{1}{\rho_1} \int_{\partial\Omega_1} v \left(\nabla P_1 \cdot n\right) dS, \end{aligned} \tag{3.17}$$

where the sifting property was applied to the Dirac operator. In addition to Eq. (3.17), the continuity of pressure, Eq. (3.5) must be directly enforced by setting $P_1 = P_2$ on $\partial\Omega_2$, and $P_1 = 0$ on $\partial\Omega_1$. Because only fluid domains are being considered (no elastic sediments) and the domains do not overlap, the subscripts for $P$ in Eq. (3.17) may be dropped, where now $P = P_1 \cup P_2$ represents the entire acoustic pressure for both domains. Dropping the subscripts and solving for the total acoustic pressure automatically ensures the continuity of pressure across the interface.

It is important to note that Eq. (3.17) is exact; no approximations were made to the governing equations. In order for the weak form to guarantee a unique and bounded solution, the product $Pv$ and $\nabla P \cdot \nabla v$ must be square integrable [46]. Mathematically, this means that $P$ and $v$ must exist in a Hilbert space, $H^1$. Also note that the surface integrals at the infinite boundaries are not included in the weak formulation. To ensure the well-posedness of the weak formulation, a weighted Hilbert space must be chosen that incorporates the Sommerfeld radiation condition in the space definition. When these weighted Hilbert spaces are used, the surface integrals at the infinite limits vanish and there are no reflected waves from the infinite bounds. More detail on weighted Hilbert spaces and well-posedness for unbounded domains can be found in chapters 2.2, 2.3 and 2.4 of [45]. Note that $v$ has not been determined yet; any function that exists in $H^1$ is allowed and will depend on the chosen variational method used to solve the weak expression. Two desirable consequences of the weak formulation are that the dependent variable only needs to

be continuous to first order derivatives, and the natural boundary conditions are automatically included.

## 3.4 Discretization

Solutions to Eq. (3.17) must be found numerically. This is done by discretizing the domain and boundaries into subdomains, called elements. In each element, $P$ and $v$ are approximated by known interpolation functions. Therefore, the solution $P$ is obtained by finding the unknown weights for each interpolation function. Many different variational methods exist, each differing by the interpolation function chosen. An extensive overview of variational methods is given in [44]. In this work, the Galerkin finite element method is used. In the Galerkin finite element method, the interpolation functions are chosen to be piecewise functions where, within a given element, $P$ and $v$ are interpolated using a Lagrange polynomial, and outside of the given element, the function is zero. This is a numerically efficient method because the matrix equation to find the unknown weights of the interpolation polynomial will be sparse and diagonally dominant.

Mathematically, the acoustic pressure is approximated by a finite series of basis functions

$$P \simeq \sum_{i=1}^{M} P_i N_i(\mathbf{x}), \tag{3.18}$$

where $P_i$ are the unknown pressures at the nodes of an element, and $N_i(\mathbf{x})$ are chosen to be Lagrange polynomials of second order. The interpolation function, $N_m$, is chosen such that the function is unity at node $i$, and zero at

the other nodes. In the Galerkin finite element method, the test function $v$ is chosen to be of the same basis function set as $P$

$$v = \sum_{j=1}^{M} N_j(\mathbf{x}). \tag{3.19}$$

Substituting Eqns. (3.18) and (3.19) into (3.17), the local matrix is obtained

$$\mathbf{A}_{\text{loc}} = \mathbf{K}_{\text{loc}} + \left(k_{1,2}^2 - k_y^2\right) \mathbf{M}_{\text{loc}}, \tag{3.20}$$

where the wavenumber is $k_1$ if the element is located in the fluid domain and $k_2$ if the element is located in the sediment domain, and

$$[\mathbf{K}_{\text{loc}}]_{i,j} = \frac{1}{\rho_{_{1,2}}} \int\limits_{\Omega_e} \nabla N_i \cdot \nabla N_j \, d\Omega_e, \tag{3.21}$$

$$[\mathbf{M}_{\text{loc}}]_{i,j} = \frac{1}{\rho_{_{1,2}}} \int\limits_{\Omega_e} N_i N_j \, d\Omega_e, \tag{3.22}$$

where $\Omega_e$ is the element domain. The local forcing matrix is

$$\mathbf{f}_{loc} = -\frac{Q(\omega)}{2\rho_1} N_j(\mathbf{x}_s) - \frac{1}{\rho_1} \int\limits_{\partial\Omega_{1,e}} \nabla N_j \left(\nabla N_i \cdot n\right) \, dS. \tag{3.23}$$

The global matrix is obtained by summing each local matrix for all elements that contain the node under consideration. After assembly, one obtains the following equations

$$\mathbf{A}P = \mathbf{F} \tag{3.24}$$

$$P_i = 0, \quad \mathbf{x}_i \in \partial\Omega_1. \tag{3.25}$$

The solution to the unknown pressures at the nodes of each element is then obtained by

$$P = \mathbf{A}^{-1}\mathbf{F}. \tag{3.26}$$

For wave propagation problems, the element size must be small enough to ensure global accuracy. At least six elements per wavelength are needed for accurate wave propagation; in this work, eight to ten elements per wavelength are used. The commercial FEM software COMSOL Multiphysics version 4.3 a/b is used for meshing and solving [52].

## 3.5 Perfectly Matched Layers

In order to accurately model infinite domains using FEM, the computational domain must be properly truncated and the Sommerfeld radiation condition must be enforced. This is often done using absorbing boundary conditions. One such absorbing boundary condition, and the one used in this work is the perfectly matched layer (PML). PMLs were originally formulated by Bérenger in [53], and have sucessfully been used in problems dealing with acoustic scattering [47].

As done by Zampolli et al. in [47], PMLs are layers an acoustic wavelength thick placed where infinite regions must be computed; for all three geometries under consideration, PMLs are placed to the left and right of both the water and sediment domains corresponding to ($-\infty \leq x \leq \infty$), and below the sediment, simulating an infinite half-space. In each PML, the spatial coordinates are transformed to complex coordinates. This transformation makes the PML dissipative in the direction of the transformed coordinate. For 2-D

Cartesian coordinates, this transformation is [52]

$$x' = \mathrm{sgn}(x - x_0)|x - x_0|\frac{\lambda_{\mathrm{ref}}}{D}(1 - i)\,, \tag{3.27}$$

$$z' = \mathrm{sgn}(z - z_0)|z - z_0|\frac{\lambda_{\mathrm{ref}}}{H}(1 - i)\,, \tag{3.28}$$

where $x'$ and $z'$ are the transformed coordinates, $x_0$ and $z_0$ are the coordinates of the inner PML boundary, $D$ and $H$ are the PML thickness and height, respectively, and $\lambda_{\mathrm{ref}}$ is the reference wavenumber, which is based on the sound speed for each domain. The conservation of pressure and normal particle velocity are enforced on the PML-computational domain interface.

# Chapter 4

# Inverse Cosine Transform

In order to calculate the total acoustic pressure field, the inverse cosine integral, Eq. (3.10), must be evaluated numerically. For a particular spatial point $(x, y, z)$, FEM must be computed for a sufficient number of independent values of the out-of-plane wavenumber $k_y$ to accurately resolve the integral. In order to compute the integral numerically, two aspects must be addressed. The first is the treatment of the infinite upper limit in the integral. The second is the selection of an efficient integral scheme. FEM computations can take on the order of minutes to solve for a single $k_y$ value; thus, a large amount of $k_y$ points can potentially be computationally unfeasible. Therefore, an efficient integral scheme must be sought that can compute the inverse cosine integral accurately to within a given tolerance and use the least amount of $k_y$ points possible. In order to address these two concerns, the properties of the integrand are first investigated. Then, two integration schemes are introduced. The first discretizes the integral into a Riemann sum. However, instead of a constant discretization in $k_y$ space, a variable discretization is used based on a gamma cumulative distribution function. The second integration scheme is a modified Clenshaw-Curtis quadrature that utilizes an adaptive algorithm such that the amount of $k_y$ values needed is minimized.

In the first section, the properties of the integrand is investigated. In the second section, the variable $k_y$ integration scheme is introduced. In the third section, the modified adaptive Clenshaw-Curtis quadrature is described.

## 4.1 Integrand Properties

To assess the qualities of the integrand, it is helpful to investigate the solution to a point source in free space at 100 Hz. This is equivalent to finding the Green's function to the transformed Helmholtz equation, Eq. 3.11. A three-dimensional solution can then be found by substituting the Green's function into the inverse cosine transform, Eq. (3.10). First, consider a source plane solution ($y = 0$). The cosine kernel is equal to one, and Eq. (3.10) becomes the integral of the Green's function over all positive $k_y$. For a source located at the origin, the Green's function, $G(k_y, r)$, of the transformed Helmholtz equation, Eq. (3.11), is [54]

$$G(k_y, r) = \begin{cases} -\frac{i}{8} H_0^{(2)}(r\sqrt{k^2 - k_y^2}), & k_y \leq k \\ \frac{1}{4\pi} K_0(r\sqrt{k_y^2 - k^2}), & k_y > k, \end{cases} \tag{4.1}$$

where $r = \sqrt{x^2 + z^2}$, and $H_0^{(2)}$ and $K_0$ are the zeroth-order Hankel and modified Bessel functions of the second kind, respectively. Note that when $k_y > k$, the form of the governing PDEs change; Eq. (3.11) is no longer the Helmholtz equation. As a result, the solution to this form of the PDE is the modified Bessel function of the second kind, which is closely related to the Hankel function with a complex argument. For $k_y < k$, the Green's function describes a propagating wave in the medium. Figure 4.1a shows solutions describing

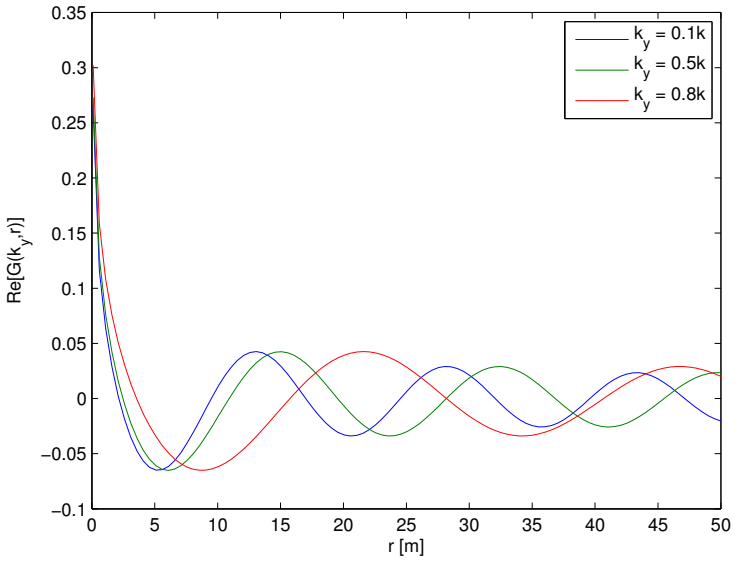


(a)

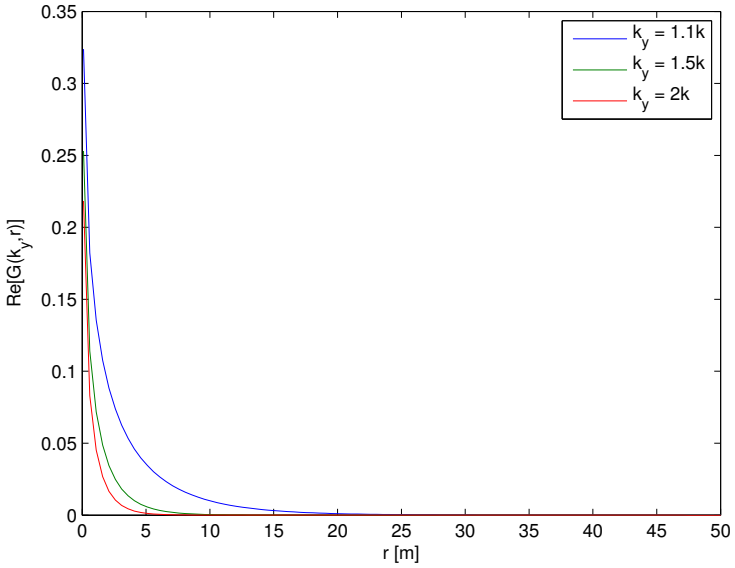


(b)

Figure 4.1: (a) Real part of the Green's function for $k_y < k$, representing propagating wave solutions. (b) Real part of the Green's function for $k_y > k$, representing evanescent wave solutions.

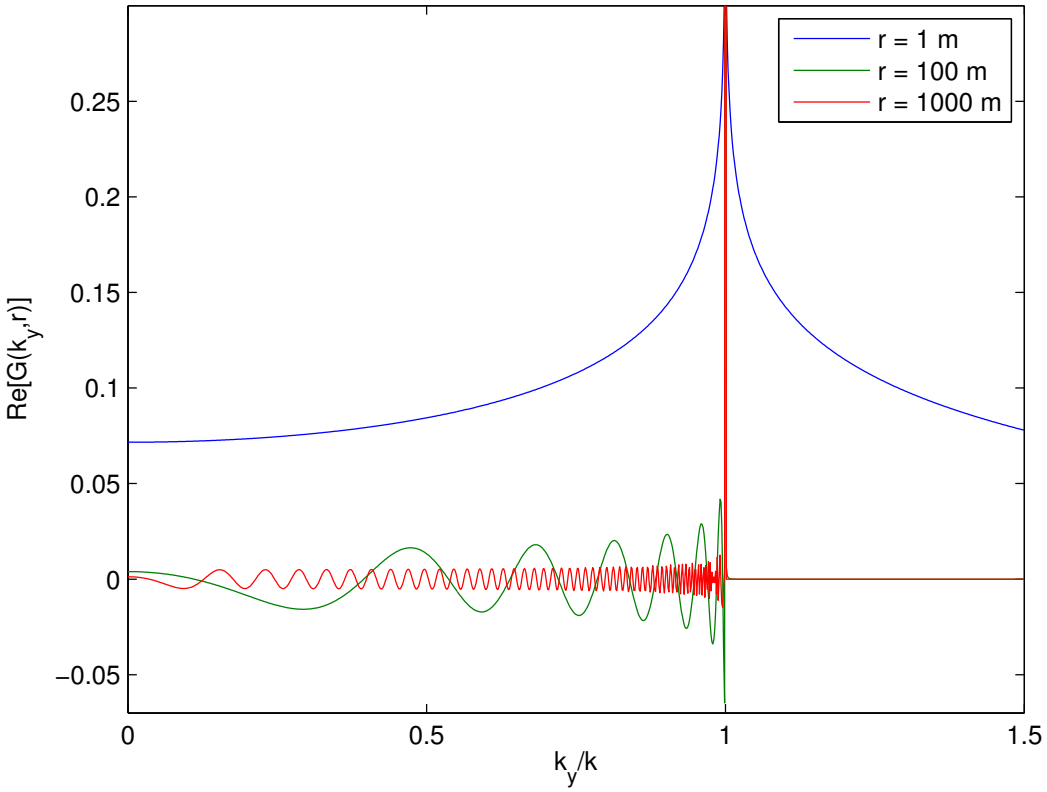


Figure 4.2: Real part of the Green's function for several range values.

propagating waves for different values of $k_y < k$. However, when $k_y > k$, the solution to Eq. (3.11) represents an evanescent wave, and no energy is propagated from the source, as shown in Fig. 4.1b. When the receiver is close to the source, the integrand exhibits high magnitude values, with low oscillations for low $k_y$ and higher oscillations when $k_y \to k$. For ranges farther away from the source, the integrand exhibits smaller magnitudes than that near the source, but the oscillations are higher. For all receiver ranges, the oscillations increase as $k_y \to k$. This is shown in Fig. 4.2. In addition, Eq. (4.1) has a singularity at

$k_y = k$. It's important to note that the Green's function describing the total acoustic pressure field for a waveguide with a penetrable bottom will have at least two singularities, one for the transition between propagation and evanescence for the compressional wave in the water, and another at the transition from propagation to evanescence for the compressional wave in the sediment. Elastic sediments can also have more than one singularity or pole, all on the real $k_y$ axis. Zhou et al. discuss the Green's function and the existence of singularities for anisotropic media in [55]. However, attenuation in the sediment displaces these singularities off of the real axis.

Next, consider 3-D solutions where $y$ is not zero. The cosine kernel is now included in the integrand and exhibits highly oscillatory behavior as $y \to \infty$. Therefore, the integrand is a product of two highly oscillatory functions. From this analysis, the two concerns stated in the introduction of this chapter can now be addressed. Since the FEM solution decays to zero once the solution to Eq. (3.11) becomes evanescent, the integrand's contribution to the integral becomes negligble past a certain wavenumber, which will be designated as the wavenumber cut-off $k_c$, and the infinite limit can be truncated to $k_c$. In addition, a constant discretization in $k_y$ will be inefficient for this integral. Since the integrand is relatively smooth for $k_y \to 0$ and gradually increases in oscillation as $k_y \to k$, a high amount of $k_y$ values are needed where the oscillations in the integrand are the strongest. Therefore, an integration scheme which has a variable spacing in $k_y$ will be the most advantageous.

## 4.2 Variable $k_y$ Integration

A numerically simple way to evaluate Eq. (3.9) is to discretize the integral into a Riemann sum:

$$p(x, y, z) = \frac{2}{\pi} \sum_{k_y=0}^{k_c} P(x, k_y, z) \cos(k_y y) \Delta k_y(k_y), \tag{4.2}$$

where $k_c$ is the cut-off wavenumber beyond which the integrand is negligible, and $\Delta k_y(k_y)$ is a function describing the spacing between adjacent $k_y$ points. $k_c$ is chosen to be in the evanescent region; for this work a value of $1.5k$ is chosen. The only parameter yet to be determined is the function describing the discretization, $\Delta k_y$. As discussed in Sec. 4.1, a variable $k_y$ spacing is desirable, where spacing between abscissa for $k_y \to 0$ is relatively large, and as $k_y \to k$ the spacing between adjacent abscissas decreases. A function which gives the position of the abscissas with the desired variable spacing is a gamma cumulative distribution function (CDF). The gamma CDF is defined as

$$k_y(\xi) = \frac{k}{b^a \Gamma(a)} \int_0^{\xi} t^{a-1} \exp(-t/b)\, dt + C, \tag{4.3}$$

where $\xi$ is a discretized variable that is evenly spaced between 0 and 1, $a$ is the shape parameter, $b$ is the scale parameter, $C$ is a constant denoting the offset, and $t$ is a variable of integration. The offset must be included such that there is a large amount of abscissas surrounding $k$. In the evanescent region, $\Delta k_y$ is chosen to be constant since the integrand is not oscillatory. In this work, the values $a = 0.8$ and $b = 0.25$ are found to give a satisfactory spacing. Figure 4.3 shows a comparison of the location of the abscissas based on Eq. (4.3) and

a constant $k_y$ spacing for 300 wavenumber values. Figure 4.4 compares the analytical solution of a point source in free space in the source plane ($y = 0$) with the solution of Eq. (4.2) using a constant $k_y$ spacing and the $k_y$ spacing based on the gamma CDF. Note that the variable $k_y$ spacing gives a more accurate result than the constant spacing.

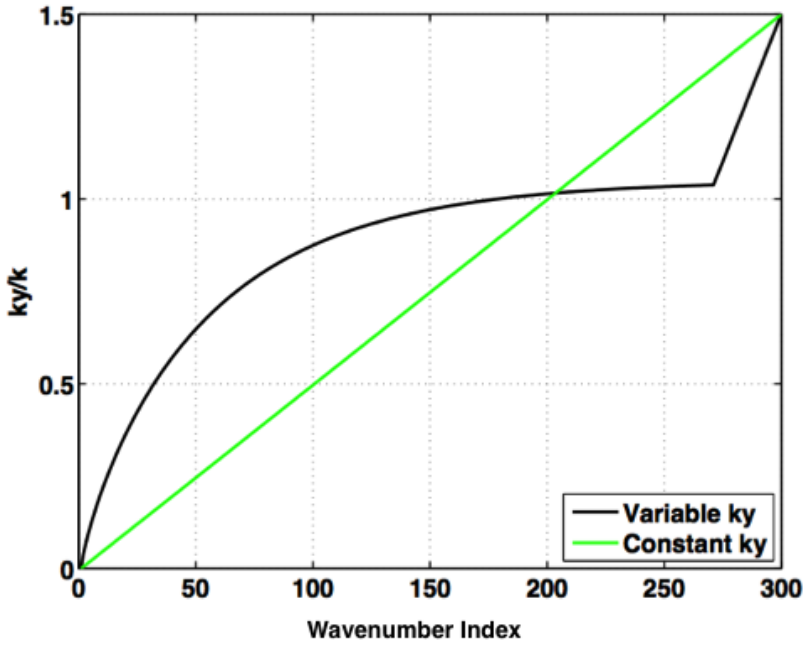


Figure 4.3: Variable $k_y$ spacing based on the gamma CDF function versus a constant $k_y$ spacing for 300 wavenumber values.

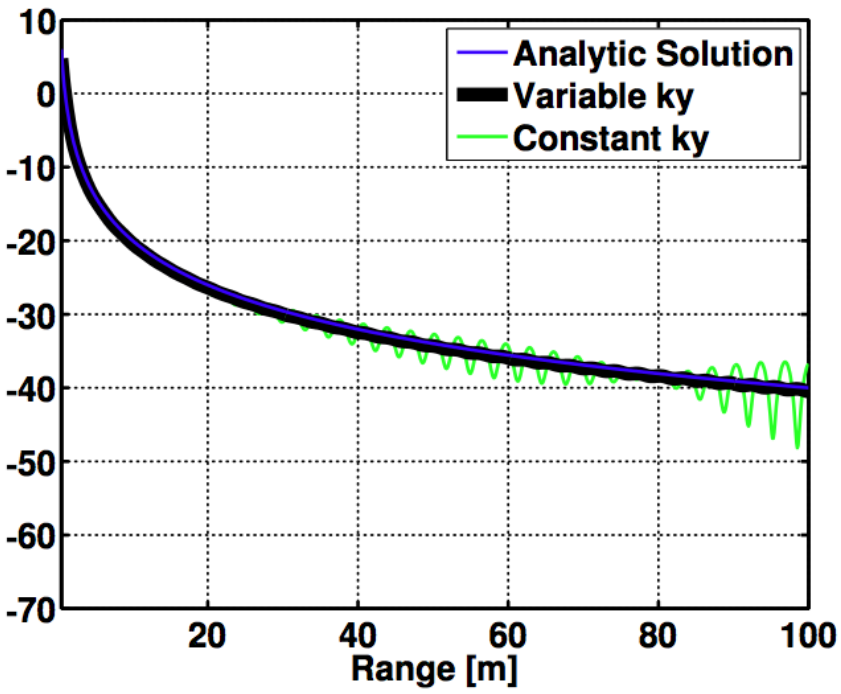


Figure 4.4: Comparison of the analytical solution to a point source in free space to the solution of Eq. (4.2) for a variable and constant $k_y$ spacing. Note that the variable $k_y$ spacing is more accurate than the constant spacing.

## 4.3 Modified Adaptive Clenshaw-Curtis Quadrature

The second integral scheme to be compared is a modified adaptive Clenshaw-Curtis quadrature. Many quadrature schemes exist to solve highly oscillatory integrands; a review of the different schemes is given in [56]. It is shown in [57] that using an adaptive integration scheme is effective for badly behaved and irregularly oscillatory integrands. It is advantageous to use an adaptive scheme in this case such that most of the abscissas are focused around regions of greatest irregularity. In addition, accuracy can be improved by using

a modest quadrature order over a series of subintervals, rather than integrating the entire limits with a high-order quadrature [58]. Therefore, an adaptive algorithm will be used to solve the inverse cosine integral, where $k_y$ space will be discretized into subintervals, and subintervals that do not converge will be subsequently bisected until the given accuracy is obtained. When performing interval subdivision, it is important to retain as many prior abscissas as possible, as this will reduce the total number of FEM evaluations necessary to compute the integral. Therefore, Gaussian quadrature schemes are not practical for interval subdivision problems since nearly all of the abscissas are lost with each interval subdivision [57]. However, certain types of quadrature schemes, such as Romberg's method and Clenshaw-Curtis retain abscissas with each interval subdivision, with little to no abscissas being lost [57].

When integrating unknown functions or discrete data, it is important to know the error of the numerical integration scheme. One way is to increase the order of the integration scheme after obtaining the value of the integral and compare the two results. If the integration limits are subdivided, then an error estimation can be done by repeating the integration with an increased number of subintervals until the values of the integral on each subinterval converge to within an acceptable tolerance. For the present work, none of these methods for determining the error are ideal because extra FEM evaluations are needed, which is computationally demanding. A mathematically rigorous way is to compute the error of a quadrature scheme a priori by investigating the residual between the approximating polynomial and the actual

function being integrated. For example, when using Gaussian quadrature of order $N$, the integration error is proportional to the $2N$ order derivative of the integrand. However, computing high order derivatives on numerical functions can be computationally demanding, again making most Gaussian quadrature schemes impractical for the present problem.

Unlike Gaussian quadratures, Clenshaw-Curtis quadrature provides an easy and conservative way to calculate the integration error. References [59–61] show that the error of Clenshaw-Curtis quadrature is bounded by the weights of the truncated Chebyshev series that approximate the integrand. Reference [62] shows that this error analysis is still accurate for product integration, such as the computation of Fourier integrals. This effective error estimation makes this integration scheme efficient for an adaptive algorithm. Depending on the Clenshaw-Curtis order used, several abscissas can be retained upon subinterval division, reducing the amount of new abscissas needed. The properties of the Chebyshev polynomials also give the potential for integral recurrence relations to compute high order quadrature; however, there are practical limitations that will be discussed below. Therefore, an adaptive Clenshaw-Curtis quadrature modified to integrate the product of the FEM solution and the cosine transform kernel is chosen and will be compared with the variable $k_y$ spacing.

Clenshaw-Curtis quadrature was first derived by Charles Clenshaw and Alan Curtis in [59]. A function which is continuous and bounded within the limits of integration can be represented by an infinte series of Chebyshev polynomials, $T_m(t)$, where $m$ denotes the order of the Chebyshev polynomial.

Chebyshev polynomials are only defined on the interval $-1 \leq t \leq 1$. By a transformation of variables, any function $f(x)$ on the interval $a \leq x \leq b$ can be rewritten as

$$f(x) = F(t) = \frac{1}{2}A_0 + \sum_{m=1}^{\infty} A_m T_m(t), \quad -1 \leq t \leq 1 \tag{4.4}$$

where

$$t = \frac{2x - (b+a)}{b+a}, \quad a \leq x \leq b \tag{4.5}$$

and

$$T_m(t) = \cos[m \cos^{-1}(t)]. \tag{4.6}$$

Chebyshev polynomials have the following orthogonal property [63]:

$$\int_{-1}^{1} \frac{T_n(t)T_m(t)}{\sqrt{1-t^2}}\, dt = \begin{cases} 0, & n \neq m \\ \pi, & n = m = 0 \\ \pi/2, & n = m \neq 0. \end{cases} \tag{4.7}$$

From the orthogonal property above, the coefficients $A_m$ are computed using the integral [64]:

$$A_m = \frac{2}{\pi} \int_{-1}^{1} \frac{F(t)T_m(t)}{\sqrt{1-t^2}}\, dt \quad m = 0, 1, 2, ... \tag{4.8}$$

Clenshaw and Curtis show in [59] that the Chebyshev series in Eq. (4.4) can be truncated to accurately represent any polynomial of degree $N$. Therefore, a function that is a polynomial of degree $N$, $f^N(x)$, can be written as

$$f^N(x) = F^N(t) = \frac{1}{2}a_0 + \sum_{m=1}^{N-1} a_m T_m(t) + \frac{1}{2}a_N T_N(t) = \sum_{m=0}^{N}{}'' a_m T_m(t), \tag{4.9}$$

where the primes in the sum denotes that the first and last terms are to be halved. To find the weights of the truncated series, $a_m$, $t$ is chosen to be the discrete points

$$t_k = \cos(\pi k/N) \quad k = 0, 1, 2, ...N. \tag{4.10}$$

The Chebyshev polynomial, Eq. (4.6), becomes $T_m(t_k) = \cos(mk\pi/N)$. $T_m(t_k)$ is substituted into Eq. (4.9), and becomes

$$\sum_{k=0}^{N}{}'' F^N(t_k) = \sum_{n=0}^{N}{}'' a_m \sum_{k=0}^{N}{}'' \cos(mk\pi/N). \tag{4.11}$$

To determine the coefficients $a_m$, both sides of equation Eq. (4.11) are multiplied by $\cos(nk\pi/N)$ and summed over $n$, resulting in

$$\sum_{n=0}^{N}{}'' \sum_{k=0}^{N}{}'' F^N(t_k)\cos(nk\pi/N) = \sum_{m=0}^{N}{}'' a_m \sum_{n=0}^{N}{}'' \sum_{k=0}^{N}{}'' \cos(mk\pi/N)\cos(nk\pi/N). \tag{4.12}$$

With the orthogonal property [59]:

$$\sum_{m=0}^{N}{}'' \sum_{n=0}^{N}{}'' \cos(\frac{mk\pi}{N})\cos(\frac{nk\pi}{N}) = \begin{cases} 0, & m \neq n \\ N, & m = n = 0 \text{ or } N \\ N/2, & m = n \neq 0 \text{ or } N, \end{cases} \tag{4.13}$$

the values of $a_m$ are given as

$$a_m = \frac{2}{N} \sum_{k=0}^{N}{}'' F^N(t_k)\cos(\frac{mk\pi}{N}), \tag{4.14}$$

$$F^N(t_k) = F[\cos(\frac{\pi k}{N})]. \tag{4.15}$$

The integral of $f^N(x)$, denoted as $I_N$, is then integral of the Chebyshev

representation of $f^N(x)$, Eq. (4.9):

$$I_N = \int_a^b f^N(x)\,dx = \frac{b-a}{2}\int_{-1}^{1} F^N(t)\,dt = \sum_{m=0}^{N}{}'' a_m \int_{-1}^{1} T_m(t)\,dt, \quad (4.16)$$

$$\int_{-1}^{1} T_m(t)\,dt = \frac{(-1)^m + 1}{1-m^2}. \quad (4.17)$$

An important recurrence relation that will be used in the subsequent sections is

$$T_0(t) = 1 \quad (4.18)$$

$$T_1(t) = t \quad (4.19)$$

$$T_{m+1}(t) = 2tT_m(t) - T_{m-1}(t) \quad (4.20)$$

Before proceeding with applying Clenshaw-Curtis quadrature to the inverse cosine transform, it is important to discuss the error associated with truncating the Chebyshev series.

### 4.3.1 Error analysis

If the function being integrated by Clenshaw-Curtis quadrature is not a polynomial of degree $N$, Eq. (4.16) will be approximate, and error will be introduced. Numerous error studies exist for Clenshaw-Curtis quadrature. Originally, Clenshaw and Curtis in [59] show that when Eq. (4.4) is a rapidly decaying series, the magnitude of the neglected higher order terms is bounded by the highest calculated weight, $a_N$. Therefore, Clenshaw and Curtis suggest using the largest of $|a_N|$, $2|a_{N-2}|$, and $2|a_{N-4}|$ as a conservative error estimate.

O'Hara et al. in [61] discuss and compare different error estimates using the Chebyshev coefficients. Following in the same manner, the goal of this section is to derive a practical and conservative error estimate using the calculated Chebyshev coefficients.

The error associated with the Clenshaw-Curtis quadrature can be derived for a class of integrals with the given form

$$\int_a^b f(x)k(x)\,dx. \tag{4.21}$$

Note that this generalized integral can be applied to the present problem by substituting $a$ and $b$ as the limits of a given subinterval in $k_y$ space, $f(x)$ as the FEM solution $P(k_y)$, and $k(x)$ as the cosine kernel $\cos(k_y y)$. The function $f(x)$ is then approximated with the truncated series, Eq. (4.9), after the change of variables given in Eq. (4.5). The truncated Chebyshev coefficients are related to the infinite series coefficients by the following [59, 60]:

$$\begin{aligned} a_m &= \frac{2}{N}\sum_{s=0}^{N}{}'' \cos(\frac{ms\pi}{N})\sum_{i=0}^{\infty}{}' A_i \cos(\frac{is\pi}{N}) \\ &= A_m + \sum_{p=1}^{\infty}\left(A_{2pN-m} + A_{2pN+m}\right). \end{aligned} \tag{4.22}$$

The integration error is found by subtracting the exact integral from the approximate

$$E = I - I_N = \int_{-1}^{1}\left(\sum_{m=0}^{N-1}{}'\left(A_m - a_m\right)T_m(t) + \left(A_N - \frac{1}{2}a_N\right)T_N(t) + \sum_{m=N+1}^{\infty} A_m T_m(t)\right)k(t)\,dt \tag{4.23}$$

Substitution of Eq. (4.22) into Eq. (4.23), with the assumption that the coefficients $A_m$ are negligible after $3N$, gives the following expression for the error [62]:

$$E = (\beta_{N+1} - \beta_{N-1})\, A_{N+1} + (\beta_{N+2} - \beta_{N-2})\, A_{N+2} + ... + (\beta_{2N} - \beta_0)\, A_{2N} + (\beta_{2N+1} - \beta_1)\, A_{2N+1} + ... + (\beta_{3N} - \beta_N)\, A_{3N}, \quad (4.24)$$

where

$$\beta_n = \int_{-1}^{1} T_n(t) k(t)\, dt. \quad (4.25)$$

Application of the triangle inequality to Eq. (4.24) produces

$$E \leq |\beta_{N+1} - \beta_{N-1}||A_{N+1}| + |\beta_{N+2} - \beta_{N-2}||A_{N+2}| + ... + |\beta_{2N} - \beta_0||A_{2N}| + |\beta_{2N+1} - \beta_1||A_{2N+1}| + ... + |\beta_{3N} - \beta_N||A_{3N}|. \quad (4.26)$$

Note that $\beta_n$ can be calculated analytically since both functions are known. Since the goal is to provide a conservative error estimate, each absolute value containing the $\beta$ terms in the above equation can be replaced by the maximum value of the $\beta$ terms, resulting in

$$E \leq \sum_{m=N+1}^{3N} \alpha |A_m|, \quad (4.27)$$

where

$$\alpha = \max\left(|\beta_{N+1} - \beta_{N-1}|, |\beta_{N+2} - \beta_{N-2}|, ...\right) \quad (4.28)$$

However, $|A_m|$ is unknown and must be approximated. Assume that $|A_m|$ approaches zero geometrically [62]:

$$|A_{N+i}| \leq c_N r_N^i, \quad 1 \leq i \leq 2N \quad (4.29)$$

where $c_N$ and $r_N$ are not yet determined constants satisfying $c_N \geq 0$, $r_N$ describes the rate of decrease, or roll-off, of the series of coefficients $A_m$, and lies in the range $0 \leq r_N \leq 1$. Substituting Eq. (4.29) into Eq. (4.27) gives

$$E \leq \sum_{i=1}^{2N} \alpha c_N r_N^i. \tag{4.30}$$

A good error estimate relies on finding adequate values for $c_N$ and $r_N$. Sloan et al. in [62] discuss finding these constants in great detail. In general, $r_N$ is straightforward to calculate if the ratio $A_{m+1}/A_m$ is fairly constant. However, usually this is not the case. If the roll-off is entirely inconsistent, $r_N$ should be assigned the conservative but safe value $r_N = 1$ (meaning that the Chebyshev coefficients are not decreasing at all). An effective method to calculate $r_N$ is outlined in [62]. It can be assumed that approximate values are available for $A_i$ for $i \leq N$, and are given as $A_i \approx a_i$ for $0 \leq i \leq N-1$ and $A_N \approx \frac{1}{2}a_N$. If the maximum order of the Chebyshev polynomial used is greater than 7 (in this work Chebyshev polynomials of order 16 are used), then $r_N$ is based on the last seven calculated weights of the truncated Chebyshev series, $a_m$. The values are separated into two subsets, $\{\frac{1}{2}a_N, a_{N-2}, a_{N-4}, a_{N-6}\}$ and $\{a_{N-1}, a_{N-3}, a_{N-5}\}$. The purpose of this division is to properly handle the cases in which the function being approximated is even or odd (if $f(x)$ is even or odd, every other coefficient vanishes). The subset with the largest element magnitude is chosen to calculate $r_N$. If the elements in the subset increase systematically, then a value of $r_N$ is chosen to be the largest ratio of successive terms. If the elements do not increase systematically, then $r_N$ is chosen to be 1. Mathematically, this

is described as the following [62]:

$$\begin{aligned} z_1 &= \max\{\frac{1}{2}a_N, a_{N-2}, a_{N-4}, a_{N-6}\}, \\ z_2 &= \max\{a_{N-1}, a_{N-3}, a_{N-5}\} \end{aligned} \tag{4.31}$$

If $z_1 \geq z_2$:

$$\text{if } |a_{N-6}| > |a_{N-4}| > |a_{N-2}| > |\frac{1}{2}a_N|, \tag{4.32}$$

$$\text{then } r_N^2 = \max\left\{\frac{|\frac{1}{2}a_N|}{|a_{N-2}|}, \frac{|a_{N-2}|}{|a_{N-4}|}, \frac{|a_{N-4}|}{|a_{N-6}|}\right\}, \tag{4.33}$$

$$\text{otherwise } r_N = 1 \tag{4.34}$$

If $z_2 > z_1$

$$\text{if } |a_{N-5}| > |a_{N-3}| > |a_{N-1}|, \tag{4.35}$$

$$\text{then } r_N^2 = \max\left\{\frac{|a_{N-1}|}{|a_{N-3}|}, \frac{|a_{N-3}|}{|a_{N-5}|}\right\}, \tag{4.36}$$

$$\text{otherwise } r_N = 1 \tag{4.37}$$

Once the roll-off parameter, $r_N$, is calculated the constant $c_N$ can be determined, assuming that Eq. (4.29) also holds for $i = 0, -1, -2, ...$, by the formula

$$c_N = \max\{|\frac{1}{2}a_N|, |a_{N-1}|r_N, |a_{N-2}|r_N^2, ..., |a_{N-6}|r_N^6\}. \tag{4.38}$$

Sloan et al. in [62] show that this error estimate works for a wide class of integrands. However, there are two ways this error estimate can potentially underestimate the true error. First, an inappropriate value of $r_N$ could be chosen if the Chebyshev coefficients exhibit a misleading pattern of rapid decline. Second, an inappropriate value of $c_N$ could be chosen if $N$ is small.

However, the only time [62] reports an underestimate of the error is for using the quadrature for a low value of $N$. Sloan et al. recommend using $N > 6$ for this error estimate to be reliable; the present work uses $N = 16$.

Now that Clenshaw-Curtis and a conservative error estimate have been derived, this quadrature scheme will now be applied to solve the inverse cosine integral, Eq. (3.10).

### 4.3.2 Modified Adaptive Clenshaw-Curtis Quadrature Applied to the Inverse Cosine Transform

We wish to compute Eq. (3.10) at a receiver point $(x_r, y_r, z_r)$ using an adaptive Clenshaw-Curtis quadrature. First, the infinite limit is truncated by $k_c$, where the contribution of the integrand is negligible (which coincides with $P$ being an evanescent wave solution to Eq. (3.11)). The integral is then divided into $M$ subintervals

$$\int_0^{k_c} (\bullet) = \int_0^{b_1} (\bullet) + \int_{b_1}^{b_2} (\bullet) + ... \int_{b_n}^{k_c} (\bullet)\,. \tag{4.39}$$

On each subinterval, Eq. (4.5) is used to change the variable of integration from $k_y$ to $t$, which changes the limits of each integral to -1 to 1. $P(t)$ is then approximated as a truncated series of Chebyshev polynomials

$$P(t) = {\sum_{m=0}^{N}}'' a_m T_m(t), \tag{4.40}$$

where the weights are defined in Eq. (4.14). The inverse cosine transform on a subinterval $[a, b]$ becomes

$$I^N = \frac{2A}{\pi} \sum_{m=0}^{N}{}'' a_m \int_{-1}^{1} T_m(t) \cos([At + B]y_r)\, dt, \tag{4.41}$$

$$A = \frac{(b_{n+1} - b_n)}{2}, \quad B = \frac{(b_{n+1} + b_n)}{2}. \tag{4.42}$$

After the implementation of trigonometric identities, Eq. (4.41) is rewritten as

$$I^N = \frac{2A}{\pi} \sum_{m=0}^{N}{}'' a_m \left[ \cos(y_r B) \int_{-1}^{1} T_m(t) \cos(Ay_r t)\, dt - \sin(y_r B) \int_{-1}^{1} T_m(t) \sin(Ay_r t)\, dt \right]. \tag{4.43}$$

After computing the weights $a_m$, error analysis from Sec. 4.3.1 is performed by computing the constants $r_N$ and $c_N$. If the error is below a given tolerance, then the integral is accepted and Eq. (4.43) is computed. However, if the error is above a certain tolerance, then the subinterval is bisected. A tolerance of $10^{-10}$ was found to provide a transmission loss error of less than 0.5 dB. Since $P$ was computed on the endpoints and the midpoint of a subinterval, these data can be reused when the subinverval is divided. However, all other abscissas must be discarded since the smaller subintervals will require new abscissas. In the present work, bisecting each subinterval is sufficient but can be improved upon; for example, considerable savings can occur by subdividing intervals based on the abscissas, such that no abscissas need to be discarded.

### 4.3.3 Considerations

One advantage of the Clenshaw-Curtis quadrature is that the error only depends on the weights of the Chebyshev polynomials, $a_m$. In other words, the error is related to how well a $N^{\text{th}}$ order Chebyshev series can approximate the FEM solution, not the product of the FEM solution and the cosine kernel. As discussed in Sec. 4.1, the cosine kernel becomes infinitely oscillatory as $y_r \to \infty$. This will require an impractical number of abscissa for large ranges using the variable $k_y$ method. However, in the Clenshaw-Curtis quadrature, the cosine kernel is distributed among the analytical integrals in Eq. (4.43). Since both $T_m(t)$ and $\cos(Ay_r t)$ are known analytic functions, the integrals can be solved exactly. Therefore, Clenshaw-Curtis quadrature is attractive for large $y_r$ values.

It is beneficial to discuss the analytical integrals in Eq. (4.43), since there is some subtlety in their evaluation. Below are integral solutions for

some of the integrals

$$\int_{-1}^{1} T_0(t)\cos(Ay_r t)\,dt = \frac{2\sin(Ay_r)}{Ay_r}, \tag{4.44}$$

$$\int_{-1}^{1} T_1(t)\sin(Ay_r t)\,dt = \frac{2\sin(Ay_r) - 2Ay_r\cos(Ay_r)}{(Ay_r)^2}, \tag{4.45}$$

$$\int_{-1}^{1} T_2(t)\cos(Ay_r t)\,dt = \frac{2\left[(Ay_r)^2 - 4\right]\sin(Ay_r) + 8Ay_r\cos(Ay_r)}{(Ay_r)^3}, \tag{4.46}$$

$$\int_{-1}^{1} T_3(t)\sin(Ay_r t)\,dt = \frac{6\left[3\,(Ay_r)^2 - 8\right]\sin(Ay_r) - 2Ay_r\left[(Ay_r)^2 - 24\right]\cos(Ay_r)}{(Ay_r)^4}. \tag{4.47}$$

There are several features to note about these solutions. First, the maximum value that any of these integral solutions can take is 2, which occurs when $Ay_r = 0$ in Eq. (4.44). For conservative error estimates, $\alpha$ in Eq. (4.28) can be chosen to be 2. For $Ay_r \to \infty$, the integral solutions decay quickly to zero, with each higher order integral converging to zero at a faster rate. However, some problems occur for $Ay_r \leq 1$. It can be shown using a series expansion of the right hand side of the above equations for $Ay_r = 0$ that the value of the integral is finite. However, numerically implementing the right hand side can cause instabilities for low values of $Ay_r$.

Since higher order Chebyshev polynomials can be found using the recurrence relation, Eq. (4.18), likewise higher order integrals can be found using a recurrence relation. Recurrence relations are derived for the product of Chebyshev polynomials and a cosine kernel in [65–68]. These recurrence relations

are stable for forward recursion only if $Ay_r > 1$. However, for small values of $Ay_r$, the recurrence relations become unstable, and Oliver's algorithm in [69] must be used. This involves having an initial and final value and constructing the recurrence relation as a tridiagonal system of equations. In the present work, it was decided to not use Oliver's algorithm for $Ay_r < 1$. Instead, the integrals in Eq. (4.43) are evaluated numerically using Matlab's built-in function, *integral*. The Matlab function *integral* approximates an integral using global adaptive quadrature while taking advantage of Matlab's vectorization of functions to reduce computational time. More information on *integral* can be found in Ref. [70]. For low values of $Ay_r$, *integral* is able to compute the integral exactly to within machine error, with little cost to speed. However, for $Ay_r > 1$, the recurrence relations are used.

# Chapter 5

# Results

The accuracy of the longitudinally invariant finite element method (LIFEM) to model underwater waveguides is now investigated. As discussed in Sec. 3.1, LIFEM is computed for three geometries. For the Pekeris waveguide and ASA wedge, there are known solutions for the transmission loss. The wavenumber integration code, Ocean Acoustic and Seismic Exploration Synthesis (OASES), provides accurate solutions for transmission loss in a Pekeris waveguide [19, 71]. The axisymmetric parabolic equation code Range-dependent Acoustic Model (RAM) is very effective in computing the transmission loss for range-dependent wedge environments with a low wedge angle, such as the ASA wedge [43, 72]. Therefore, LIFEM will be compared with these two models to determine the accuracy of LIFEM to predict transmission loss in underwater waveguides. However, no vetted models yet exist at the time of this writing that give an exact solution to the transmission loss for the underwater Gaussian canyon; only computational models with inherent physical assumptions to the governing equations exist [73, 74]. However, due to the mathematical formulation of LIFEM, particularly the fact that no physical assumptions to the governing equations are made, the solution is accurate for any general longitudinally invariant environment as long as the size of each element is sufficiently

small and enough out-of-plane wavenumbers are used to compute the inverse transform. Therefore, the Gaussian canyon is shown to demonstrate the ability of LIFEM to model complex 3-D acoustic phenomena that is present in this type of underwater environment.

In addition to the accuracy of LIFEM, the variable $k_y$ method and the modified adaptive Clenshaw-Curtis quadrature (MACC) are compared in terms of accuracy and number of $k_y$ values (or, equivalently, the number of 2-D field evaluations) needed to compute the inverse cosine transform. The difference in the computed transmission loss between the two integration schemes and the total number of FEM evaluations are compared for each waveguide.

## 5.1 Pekeris Waveguide

First, the range-independent Pekeris waveguide discussed in Sec. 3.1 is investigated for a frequency of 100 Hz. This study serves two purposes. The first is to assess the accuracy of the computation of the transmission loss using LIFEM, and the second is to analyze the strengths and weaknesses of the two integration schemes. To address the first issue, LIFEM is compared to the wavenumber integration code, OASES, using both integration schemes. The transmission loss is first compared in the source plane ($y = 0$), where the cosine kernel has no effect on the inverse cosine transform, such that the accuracy of LIFEM can be assessed. Figure 5.1a shows the comparison between LIFEM and OASES at a depth of 24 m, and Fig. 5.1b shows the comparison between LIFEM and OASES at a depth of 98 m. LIFEM, computed with

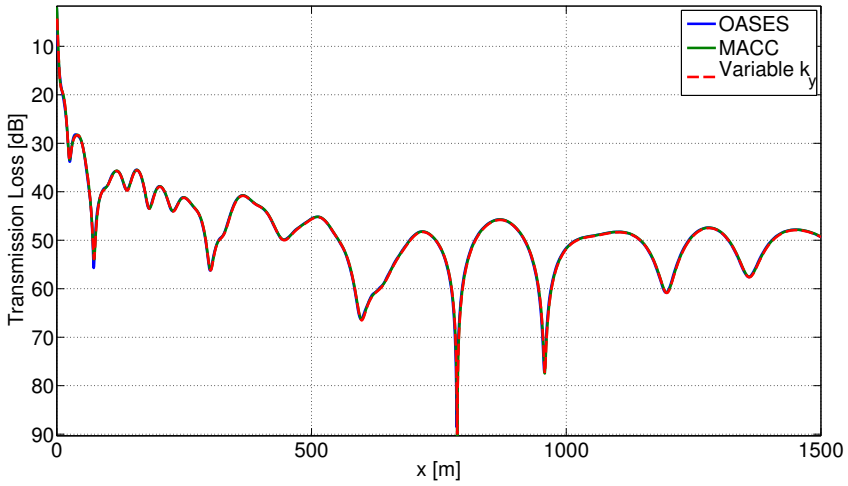


(a)

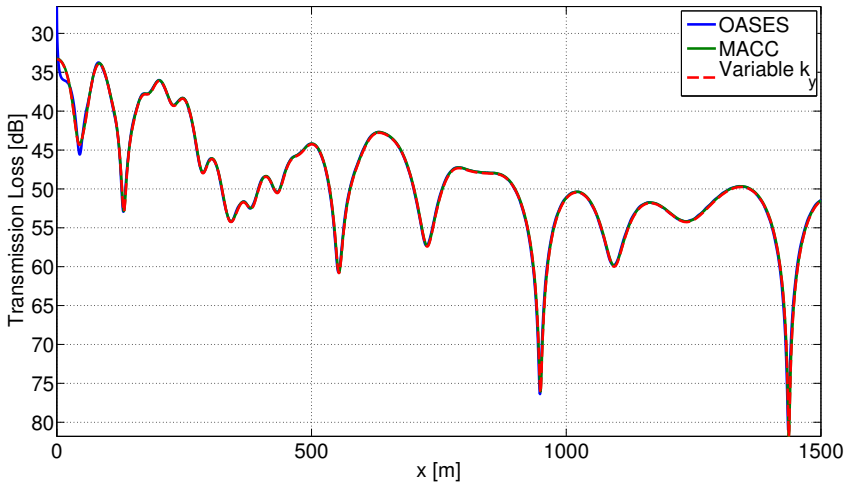


(b)

Figure 5.1: Comparison of the variable $k_y$ method, modified adaptive Clenshaw-Curtis quadrature (MACC), and the wavenumber integration code OASES in the source plane ($y = 0$) at a depth of (a) 24 m, (b) 98 m.

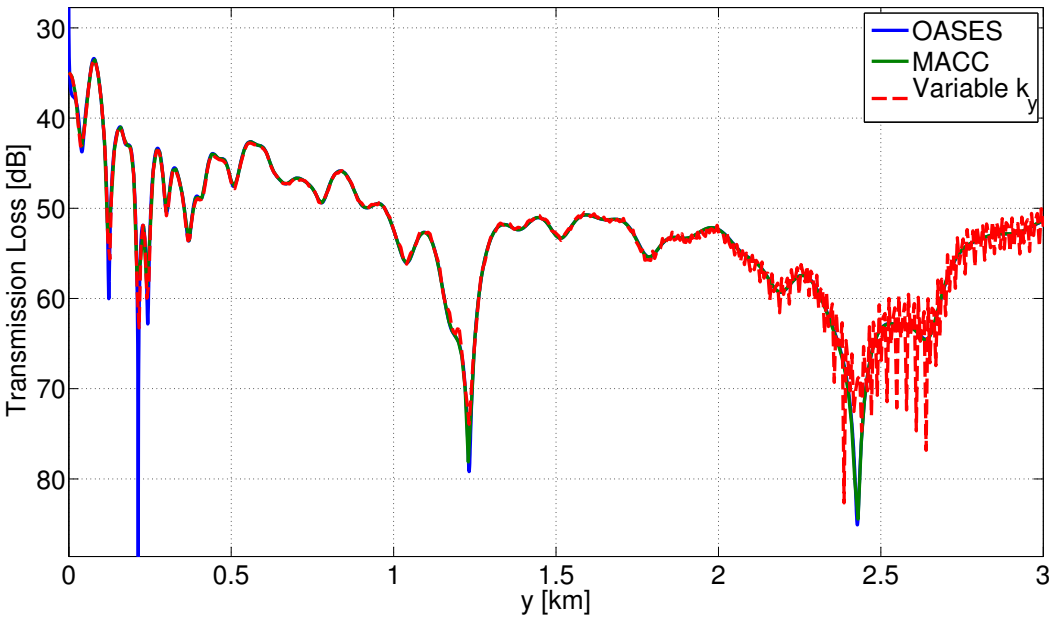


Figure 5.2: Comparison of the variable $k_y$ method, modified adaptive Clenshaw-Curtis quadrature (MACC), and the wavenumber integration code OASES along the invariant coordinate $y$ at a depth of 89 m.

either integration scheme, agrees with OASES with excellent precision. It is important to note the total number of $k_y$ abscissas needed for both integration schemes to compute the source plane solution. The variable $k_y$ method was computed with 3100 $k_y$ values, and upon completion of the adaptive algorithm with the prescribed error tolerance of $10^{-10}$, MACC used 10365 $k_y$ values. Therefore, for source plane solutions ($y = 0$), the variable $k_y$ method produced accurate results using fewer $k_y$ evaluations than MACC.

Next, the accuracy of the two integration schemes in computing the transmission loss along the invariant coordinate $y$, at $x = 0$ is investigated. The

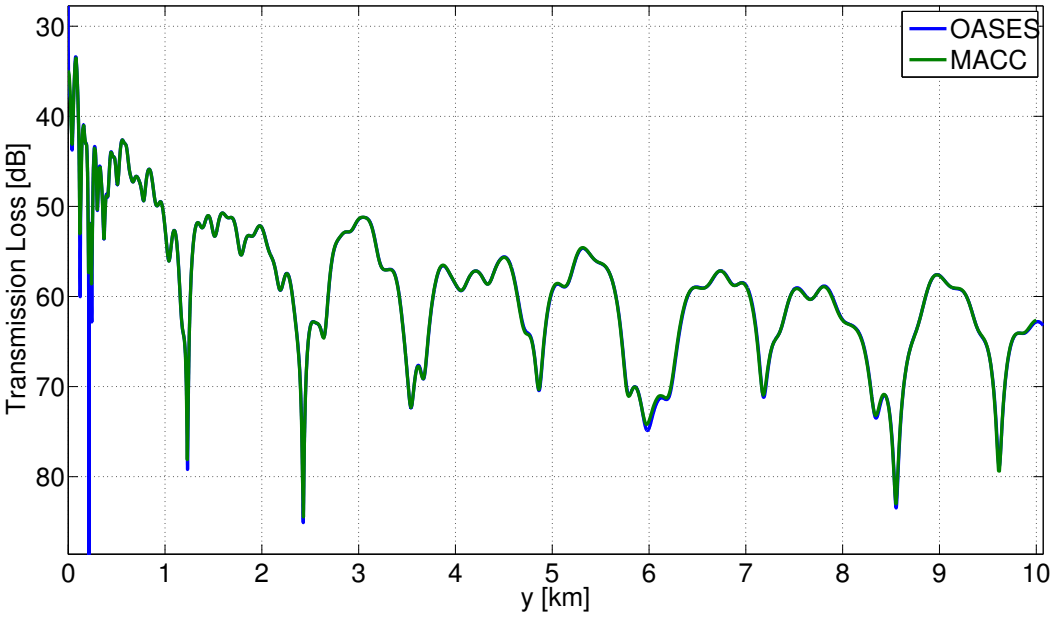


Figure 5.3: Modified adaptive Clenshaw-Curtis quadrature (MACC) compared with the wavenumber integration code OASES along the invariant coordinate $y$ at a depth of 89 m.

abscissas used to compute the source plane solution were used without adding any new abscissas to determine the effect of the cosine kernel on the accuracy of the two integration schemes. Figure 5.2 compares the two integration schemes with OASES in the invariant direction at a depth of 89 m. Note that the variable $k_y$ method produces accurate results until 1.5 km; past this range the solution becomes oscillatory about the exact solution. Since the cosine kernel increases in oscillation in $k_y$ space as $y$ increases, there is an invariant range value where the used abscissas for the variable $k_y$ method undersamples the cosine kernel. When the cosine transform is undersampled, the computed

transmission loss becomes oscillatory and inaccurate for large values of $y$. To obtain more accurate solutions along $y$, more abscissas are needed to properly sample the cosine kernel. In contrast, MACC matches the OASES solution accurately for large values of $y$, as shown in Fig. 5.3. This is due to the fact that the cosine kernel is transferred to an integral that is solved explicitly. Therefore, the accuracy of MACC is retained for large values of $y$ without the need for additional abscissas.

## 5.2 ASA Wedge

The ASA wedge is now computed using LIFEM at a frequency of 25 Hz. First, the accuracy of LIFEM is considered by comparing the computed transmission loss with an axisymmetric parabolic equation code, RAM [72]. Because RAM is an axi-symmetric model, only the source plane can be compared with LIFEM. Figure 5.4 shows the comparison between LIFEM using MACC and RAM (the variable $k_y$ method produced identical transmission loss to MACC) in the source plane. This figure shows great agreement between LIFEM and RAM. Figure 5.5 shows the source plane transmission loss using the variable $k_y$ method. Since this environment is range-dependent, 3-D acoustic phenomena are present in this model. When a mode propagating upslope reaches its cut-off depth, the modal energy is transferred into the sediment as a distinct beam of energy. Therefore, a shadow region exists near the wedge apex. In addition, horizontal refraction effects exists for modes propagating at oblique incidence to the wedge apex. This effect is shown in Fig. 5.6, which

displays a "top down" view ($xy$ plane) of the transmission loss at depths of 30 m and 100 m, respectively. Note that the energy refracts down towards the deeper water, and there exists shadow zones where little acoustic energy enters. This can be compared qualitatively with Fig. 7 of [32], although note that the source is closer to the wedge apex.

Next, the two integration schemes are compared. Figure 5.7 shows the transmission loss along the $y$ coordinate at $x = 0$, for depths of 30 m and 150 m, respectively. Note that MACC computed a more accurate solution for larger distances in $y$ compared to the variable $k_y$ method, which was also seen in the Pekeris waveguide solution. In Fig. 5.7b the difference in the two solutions exceed more than 0.2 dB for $y > 3$ km. In addition, MACC used 4370 FEM evaluations, while the variable $k_y$ used 6100 FEM evaluations. Therefore, MACC outperformed the variable $k_y$ method in both accuracy and efficiency.

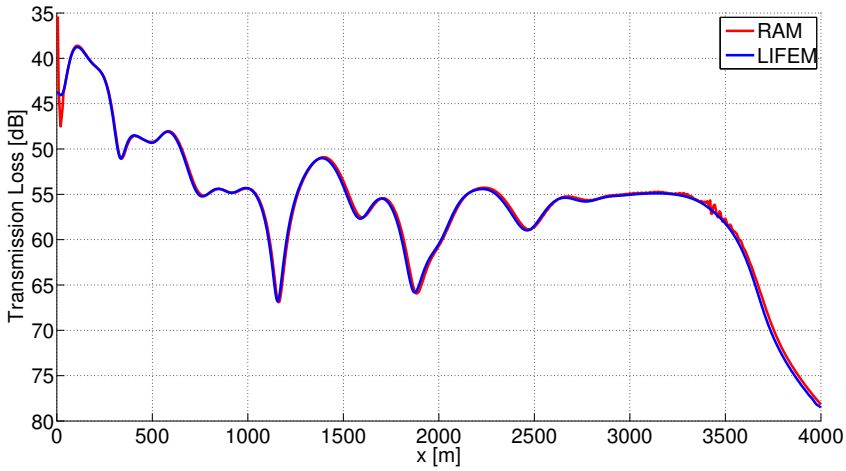


(a)

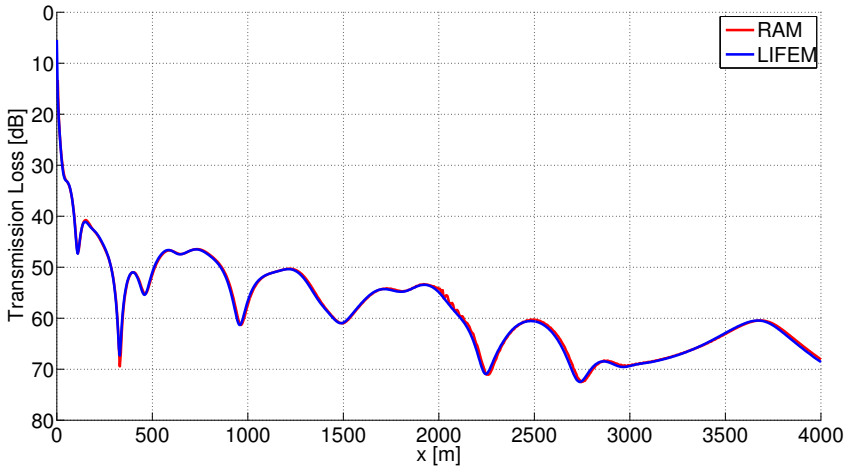


(b)

Figure 5.4: Longitudinally invariant finite element method (LIFEM) versus the axi-symmetric parabolic equation code RAM in the source plane ($y = 0$) at a depth of (a) 30 m, and (b) 100 m.

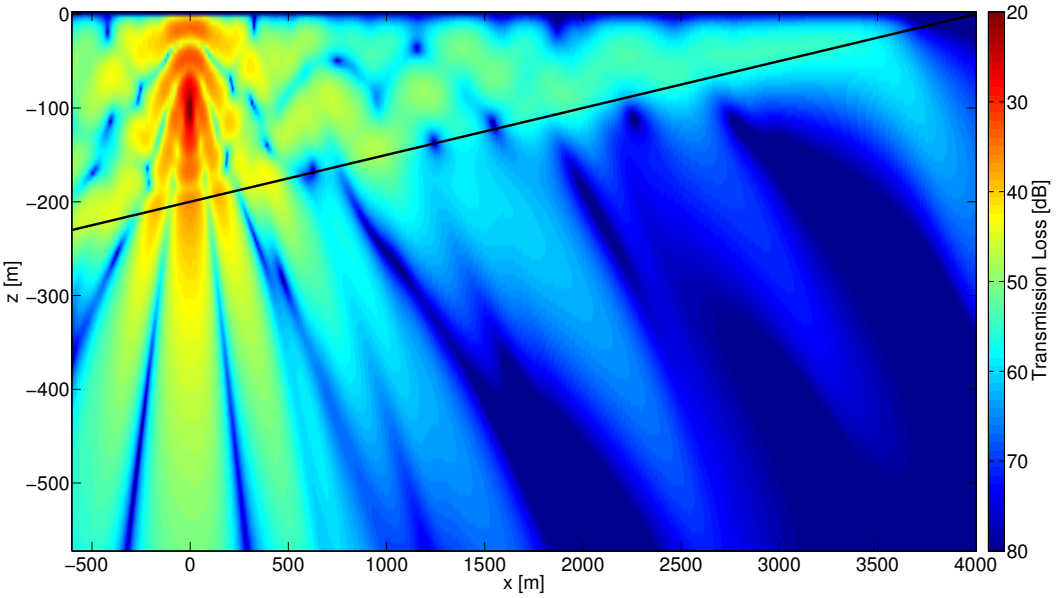


Figure 5.5: Source plane transmission loss computed using the variable $k_y$ method.

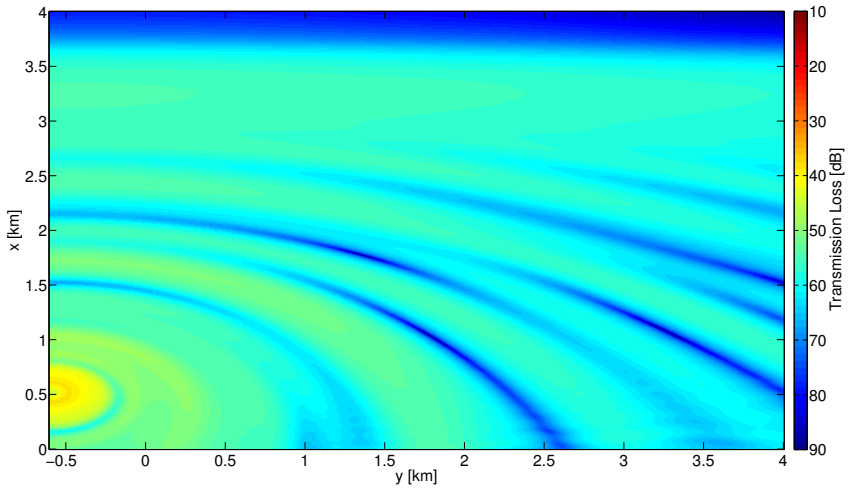


(a)

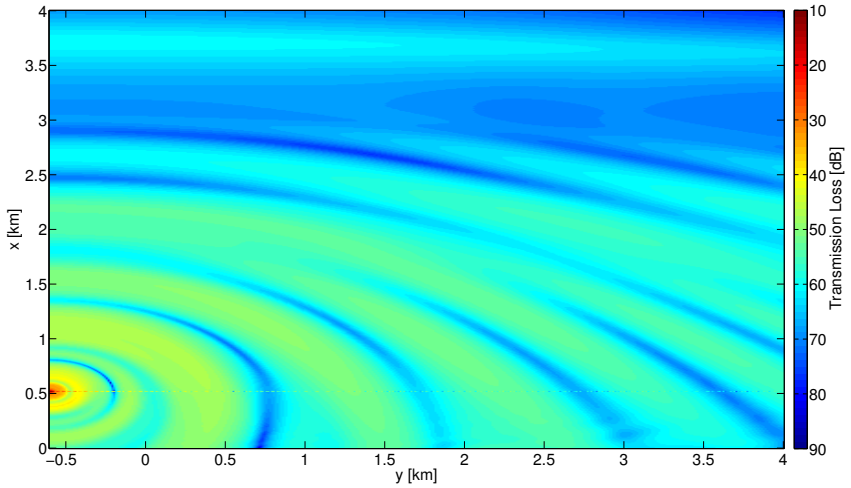


(b)

Figure 5.6: "Top down" view of the ASA wedge at a depth of (a) 30 m, and (b) 100 m.

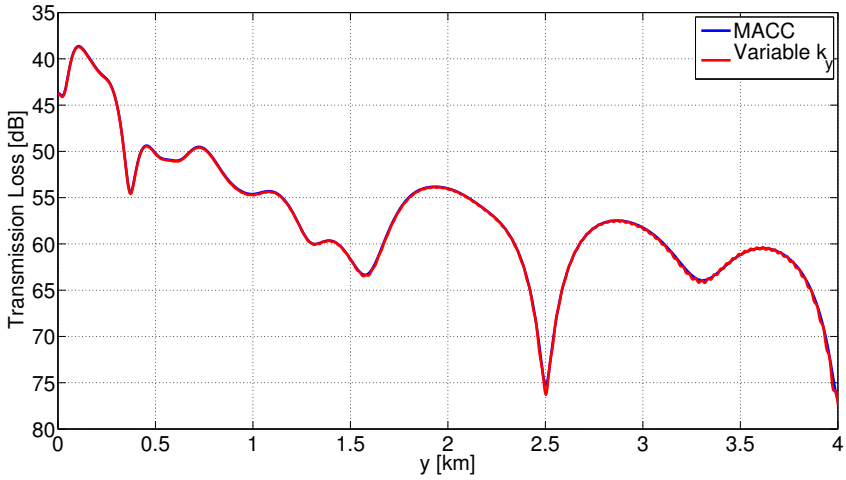


(a)

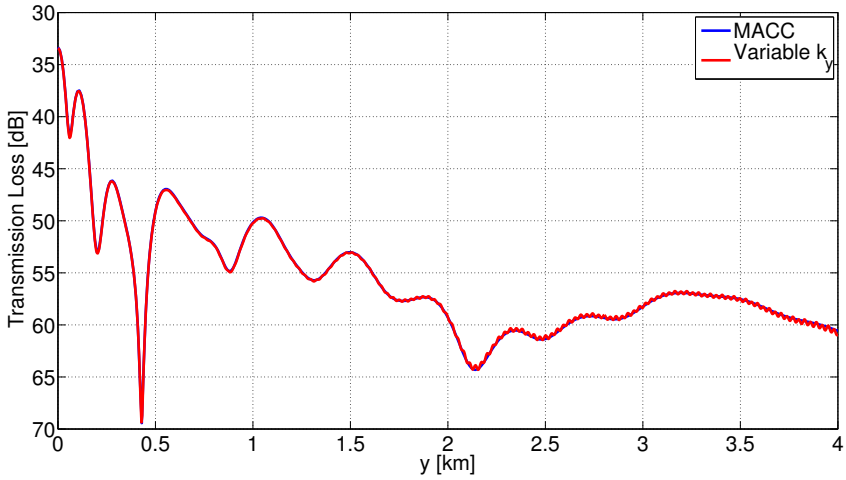


(b)

Figure 5.7: Comparison of the variable $k_y$ and modified adaptive Clenshaw-Curtis quadrature (MACC) for the ASA wedge along the invariant coordinate $y$ at $x = 0$, and at a depth of (a) 30 m, and (b) 150 m.

## 5.3 Gaussian Canyon

The final geometry considered is the Gaussian canyon waveguide at a frequency of 25 Hz. Figure 5.8 shows the transmission loss in the source plane using the variable $k_y$ method. Physically, there exists a complex interference pattern caused from the reflected field due to the concave ocean bottom, and a zone of high transmission loss directly below the source. This zone is due to the Lloyd's mirror effect, since the source is located exactly half an acoustic wavelength from the air-water interface. Figure 5.9 shows a "top down" view of the canyon ($xy$ plane) using MACC at a depth of 10 m, 35 m, 100 m, 150 m, and 180 m, respectively. There are primarily two important physical phenomena present. The first is the existence of horizontal refraction. As the energy propagates upslope to the canyon, the energy refracts down towards the deeper water. Close to the source, the modes steeply refract and interfere with themselves, causing intermodal interference. This is seen in the first few kilometers in the $y$ direction. Also, due to the perfect symmetry of the canyon about the $x = 5000$ axis, horizontal refraction exists on both sides. Therefore, the second acoustic phenomenon is a strong energy focusing effect present at $y \approx 12$ km. After this region, the modal energy refracts again into a complex constructive and destructive interference pattern.

The two integration schemes are now compared for the Gaussian canyon. MACC used 26712 FEM evaluations and the variable $k_y$ spacing used 20149 FEM evaluations. Figure 5.10 compares MACC with the variable $k_y$ method in the source plane at depths of 35 m and 130 m, respectively. Note that the

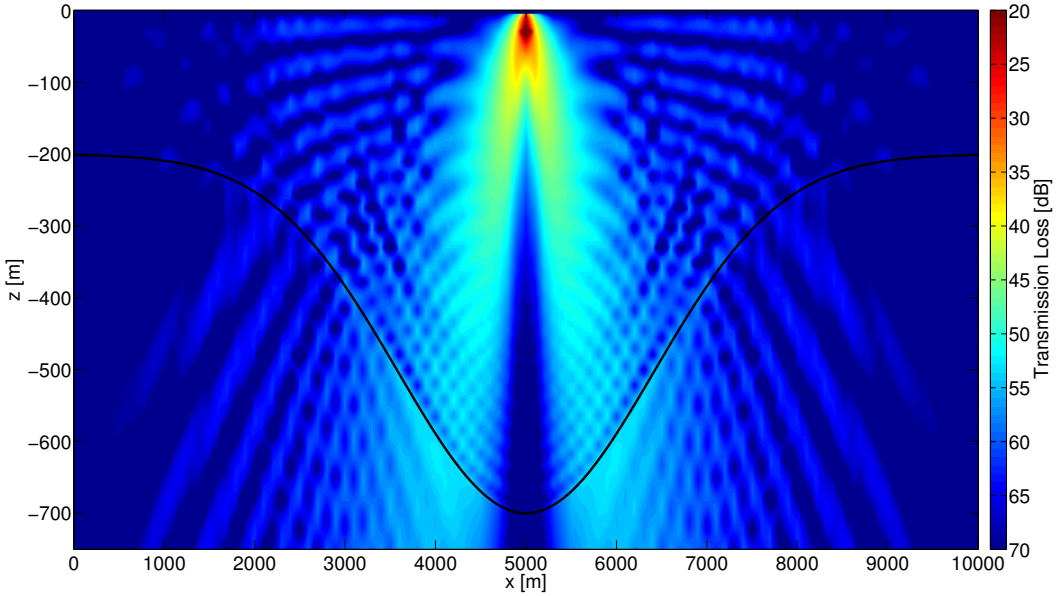


Figure 5.8: Source plane solution to the Gaussian canyon using the variable $k_y$ method.

two methods compute identical transmission loss curves. Figure 5.11 compares the two integration schemes along the canyon beginning at the source location ($x = 5000$ m) at depths of 30 m and 35 m, respectively. In Fig. 5.11a, the transmission loss computed with the variable $k_y$ method exhibits highly oscillatory nature in the first few kilometers. Because there is no *a priori* error estimate in the variable $k_y$ method, it is hard to know where in $k_y$ space more abscissas are needed. The only way to make the solution converge is to either compute more abscissas at the midpoint between prior abscissas, which is computationally inefficient, or make an educated guess on where more abscissas are needed. In contrast, the adaptive algorithm in MACC placed the abscissas

in the necessary areas, causing the solution to convergence to a smooth transmission loss curve. Figure 5.11b shows similar behavior until $y \approx 3$ km, then the variable $k_y$ method produces a smooth transmission loss curve identical to the MACC curve.

Due to the fact that the evanescent components of Eq. (3.2) decay for ranges along $x$ away from the source, the variable $k_y$ method should perform well along the $y$ direction away from the source $x$ axis. Figure 5.12 shows the solutions of the two integration schemes as a function of the invariant direction $y$ at a depth of 35 m, and at a distance of 1000 m away from the source in the $x$ plane ($x = 6000$ m) and 2000 meters away from the source in the $x$ plane ($x = 7000$ m), respectively. As predicted, these two figures show that the variable $k_y$ method and MACC agree.

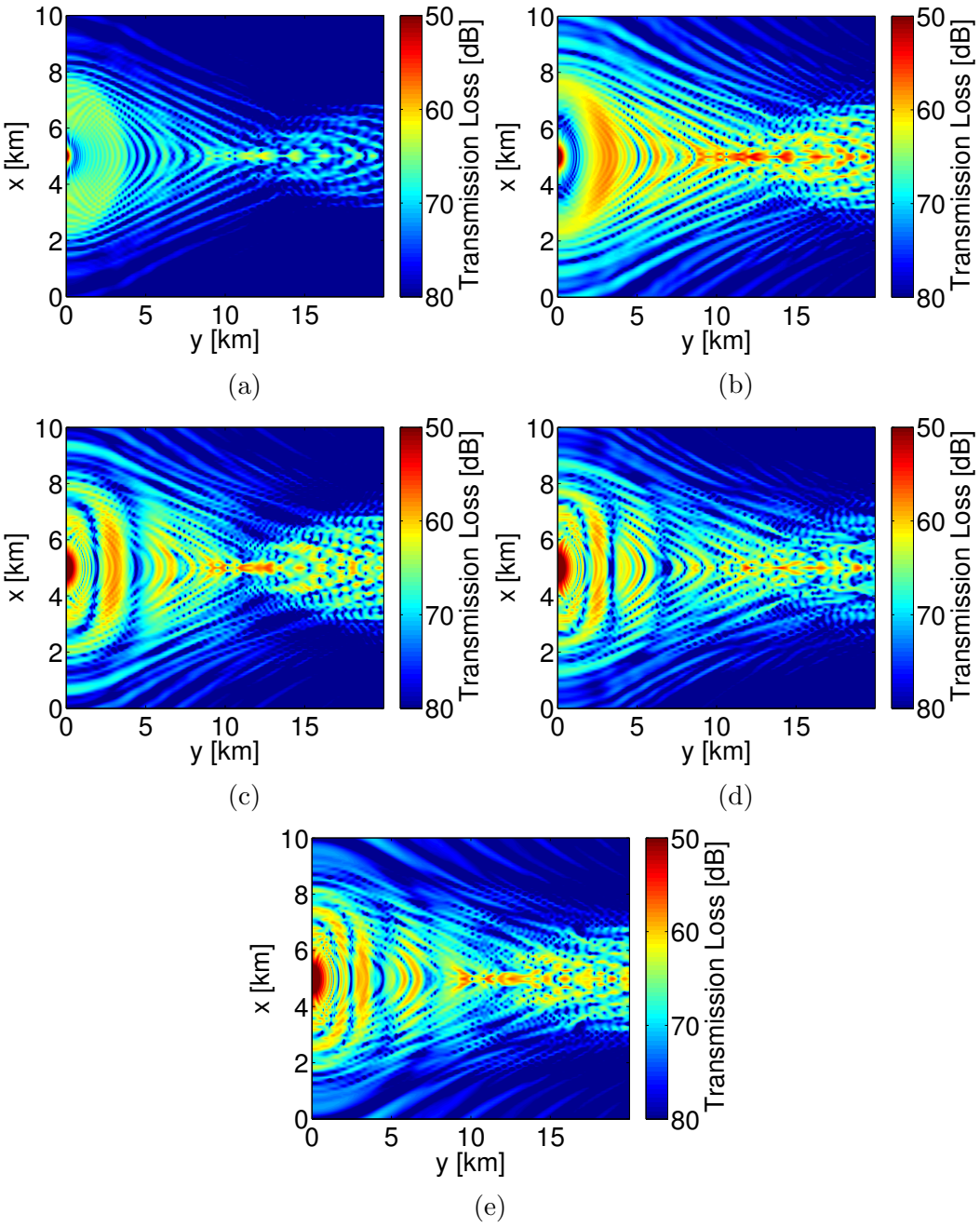


Figure 5.9: "Top down" view of the Gaussian canyon at a depth of (a) 10 m, (b) 35 m, (c) 100 m, (d) 150 m, and (e) 180 m.

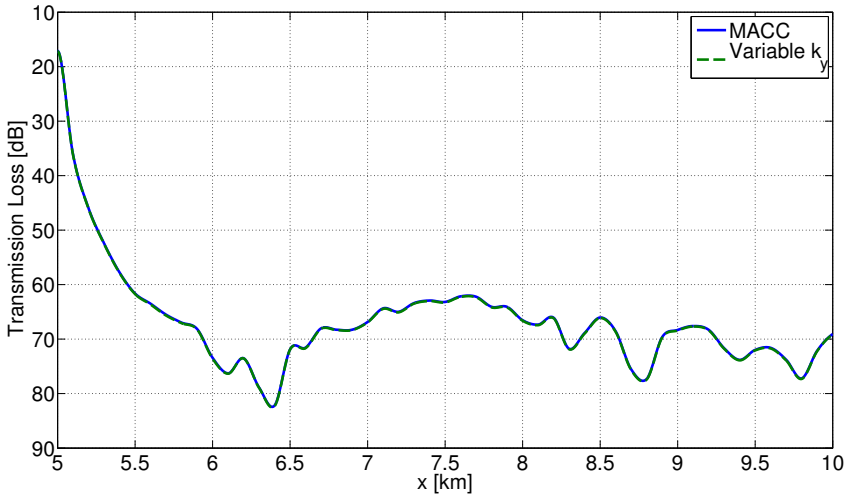


(a)

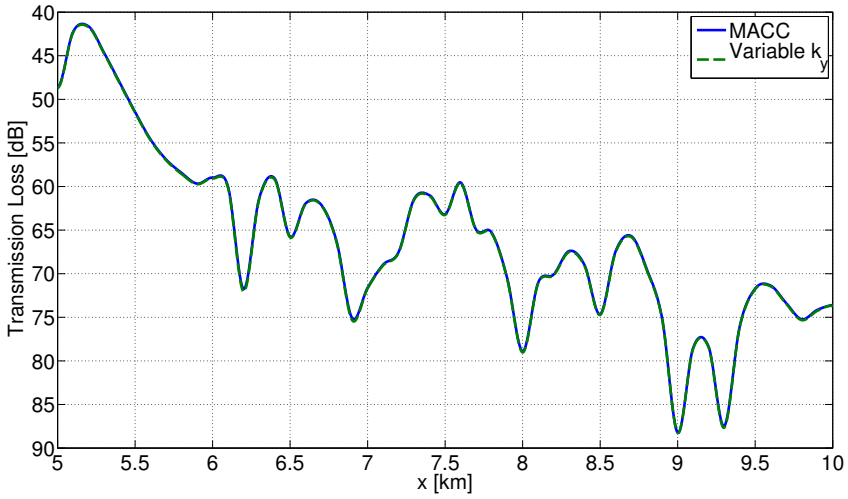


(b)

Figure 5.10: Comparison of modified adaptive Clenshaw-Curtis quadrature (MACC) and the variable $k_y$ method for the Gaussian canyon in the source plane ($y = 0$), and at a depth of (a) 35 m, and (b) 130 m.

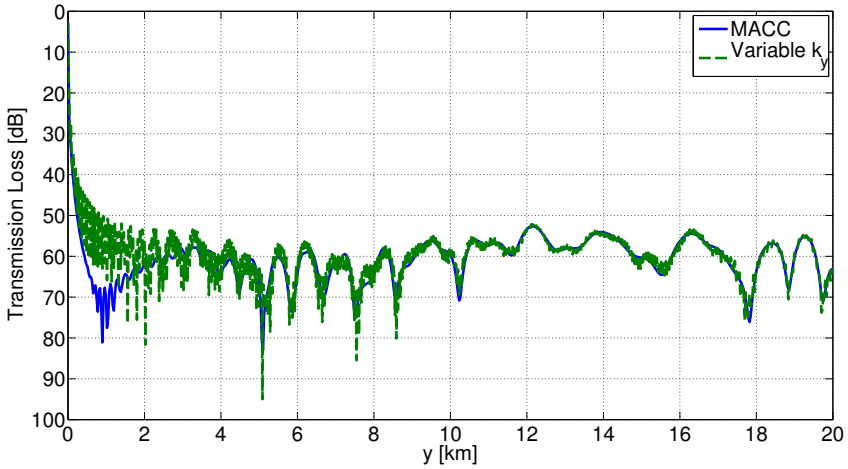


(a)

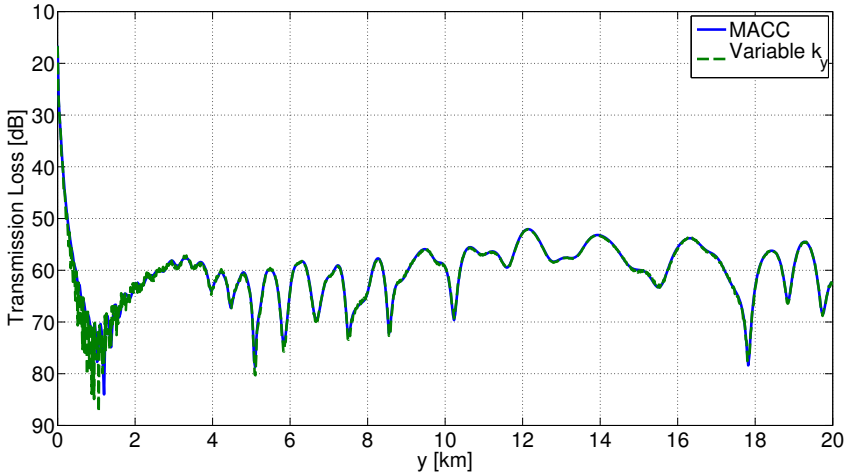


(b)

Figure 5.11: Comparison of the variable $k_y$ and modified adaptive Clenshaw-Curtis quadrature (MACC) for the Gaussian canyon along the $y$ coordinate at the source location ($x = 5000$ m), and at a depth of (a) 30 m, and (b) 35 m.

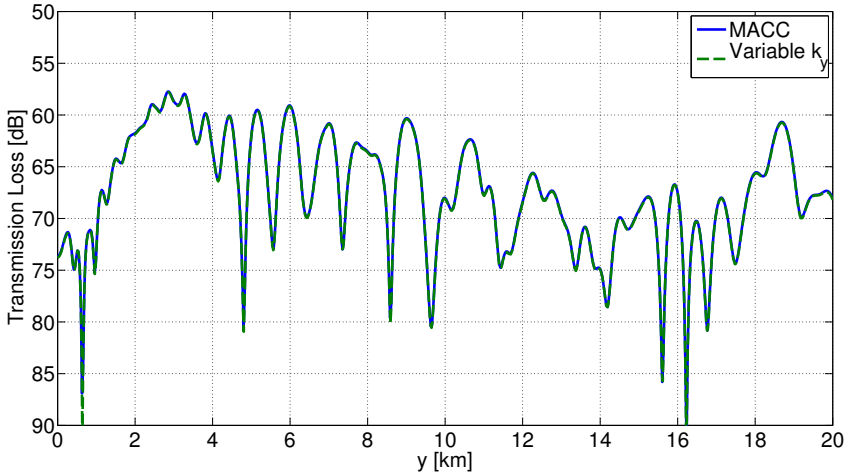


(a)

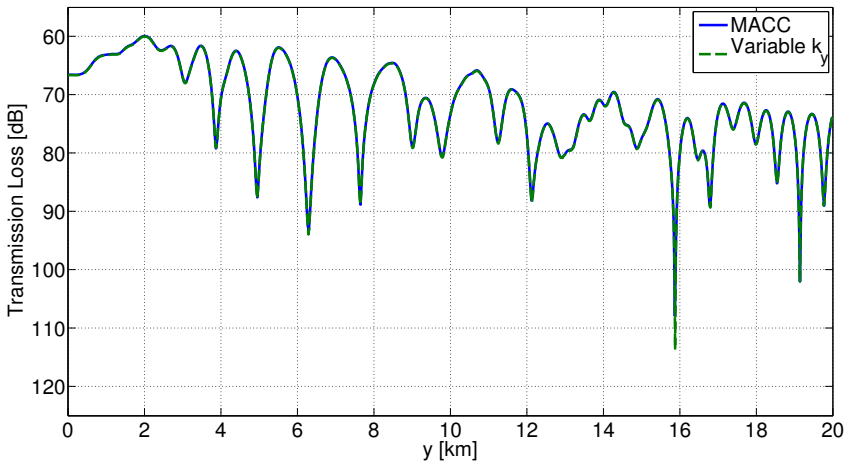


(b)

Figure 5.12: Comparison of the variable $k_y$ and modified adaptive Clenshaw-Curtis quadrature (MACC) for the Gaussian canyon along the $y$ coordinate at a depth of 35 m and (a) 1000 m from the source ($x = 6000$ m), and (b) 2000 m from the source ($x = 7000$ m).

# Chapter 6

# Conclusion

This work employed the finite element method to model three-dimensional range-dependent waveguides. In particular, a longitudinally invariant finite element model was presented, in which a three-dimensional acoustic pressure field can be computed with multiple two-dimensional finite element models for different out-of-plane wavenumbers if the bathymetry does not vary along one Cartesian spatial coordinate. Two questions were presented in the introduction, and are now answered in turn.

1. **How accurate is the longitudinally invariant finite element method in computing the transmission loss in a three-dimensional range-dependent waveguide?**

The longitudinally invariant finite element method was computed for three different waveguides. The first waveguide was a flat, range-independent Pekeris waveguide. OASES, a wavenumber integration code, provides exact solutions to Pekeris waveguides up to machine precision [19, 71]. As shown in Sec. 5.1, LIFEM agreed excellently with OASES for both source plane solutions ($y = 0$) and along the invariant direction. The second waveguide considered was the ASA wedge environment. RAM, an axi-symmetric parabolic equation

code, provides accurate solutions for source plane acoustic propagation [43, 72]. Therefore, RAM was used as a comparison for LIFEM in the source plane. As shown in Sec. 5.2, LIFEM is able to provide accurate solutions to upslope wedge propagation. In addition, the three-dimensional effects were qualitatively compared to a virtual source image method, Fig. 7 of [32], and both exhibit similar features. Finally, an underwater Gaussian canyon was computed. Unlike currently existing models, LIFEM is able to calculate the pressure field exactly. As a result, LIFEM can be used as a benchmark for other propagation models that are approximate.

2. **What is an efficient integration scheme that uses the least number of finite element evaluations and calculates the inverse transform accurately?**

Two integration schemes were developed in Chapter 4. The first discretizes the inverse cosine transform into a Riemann sum. However, abscissas with constant spacing do not compute the integral accurately and efficiently. This is due to the fact that the integrand is irregularly oscillatory, with the greatest variation near $k_y \to k$. For that reason, having a variable spacing, in which the most abscissas are located at $k_y \to k$, is advantageous. It was found that using a gamma cumulative distribution function, Eq. (4.3), gives the placement of the abscissas with the desired spacing. Indeed, Fig. 4.4 shows that for a point source in free space the variable spacing integration scheme

provides a more accurate solution than the constant spacing scheme, using the same amount of abscissas.

A modified adaptive Clenshaw-Curtis quadrature (MACC) was also developed to compute the inverse cosine transform. By approximating the FEM solution in the inverse cosine integrand as a $N^{th}$ order Chebyshev polynomial, the oscillatory cosine kernel is transferred to an integral that is solved explicitly. In addition, the Chebyshev polynomial coefficients can be used as a conservative error estimation. The adaptive algorithm places the Chebyshev abscissa around the regions of greatest oscillation in the FEM solution.

In chapter 5, the two integration schemes were compared for each of the three waveguides. For the Pekeris and Gaussian canyon waveguides, the variable $k_y$ spacing integration scheme was able to produce accurate solutions using fewer abscissa than MACC in the source plane ($y = 0$). In addition, the variable $k_y$ spacing was able to provide accurate solutions along the invariant direction for the Pekeris waveguide, ASA wedge, and Gaussian canyon away from the source $x$ axis (Fig. 5.12), while using less abscissa than MACC for the ranges considered. However, Fig. 5.2 suggests that there will be an invariant range value in which the product of the FEM solution and the cosine kernel will be undersampled by the variable $k_y$ method. In contrast, MACC does not suffer from this problem. This is due to the fact that the precision of MACC only depends on the accuracy of interpolating the FEM solution in $k_y$ space with Chebyshev polynomials, not the product of the FEM solution and the cosine kernel. Once the FEM solution has been accurately interpolated with

Chebyshev polynomials, the integration scheme will be accurate for any value of $y$. Therefore, for ranges considered in this work, the variable $k_y$ spacing provides an accurate solution for a practical number of abscissa. However, for ranges larger than those considered in this work, MACC should be considered.

# Appendices

# Appendix A

# Modified Adaptive Clenshaw-Curtis Quadrature Algorithm

A simple example of the modified adaptive Clenshaw-Curtis algorithm, in particular the adaptive procedure and the Chebyshev interpolation of the integrand, is presented. As presented in Sec. 4.3, Clenshaw-Curtis quadrature is equivalent to interpolating the integrand with an $N^{th}$ order Chebyshev polynomial, and integrating that representation. We will consider the integration of the inverse cosine transform of a point source in free space at a distance of 100 m in the source plane ($y = 0$), such that the cosine kernel has no effect on the integrand. The integrand in $k_y$ space is shown in Fig. 4.2. Since the integrand does not contribute to the integral past $k_y = 1.5k$, $k_c$ is chosen to be $1.5k$. For the purpose of illustration, the initial number of subintervals is chosen to be 2, and a $16^{th}$ order Chebyshev polynomial is used to interpolate the integrand. As a result, the first integral will be computed from 0 to $k_c/2$. Figure A.1c compares Chebyshev, Lagrange, and linear interpolation with the exact integrand. For a set of data points $[(x_0, y_0), \ldots, (x_k, y_k)]$, Lagrange in-

terpolation is defined as

$$L(x) = \sum_{j=0}^{k} y_j \phi_j(x) \tag{A.1}$$

$$\phi(x) = \prod_{\substack{0 \le m \le k \\ m \ne j}} \frac{x - x_m}{x_j - x_m}. \tag{A.2}$$

Figure A.1b shows the percent error of the interpolation over this interval. Note that linear interpolation yields the largest error. Lagrange interpolation produces the least error in the midpoint of the subinterval, but exhibits Runge's phenomena, which is numerical error that exists at the endpoints of a subinterval when a polynomial of high degree is used to approximate a function [75]. Chebyshev interpolation maintains a low error for the entire subinterval. It was shown in Sec. 4.3.1 that the error of the integration (and the error in interpolation) is bounded by the weights of the Chebyshev polynomials. Figure A.1c shows the magnitude of of the Chebyshev coefficients. Note that the weights past $|a_8|$ begin to decay. This means that the Chebyshev series is converging, and will provide an accurate integral solution. The number of significant figures of precision is dependent on the error tolerance the user supplies. The error for this case, after computing $r_N$ and $c_N$, is $7.36 \times 10^{-4}$. Because this is greater than the prescribed tolerance $10^{-10}$, the integration is not preformed and the subinterval will be bisected.

Next, the second subinterval, from $k_c/2$ to $k_c$, is computed. Figure A.2a compares Chebyshev, Lagrange, and linear interpolation with the exact function. Note that none of interpolation schemes accurately interpolate the

integrand. The magnitude of the Chebyshev coefficients is shown in Fig. A.2b. Note that the the Chebyshev coefficients are not decaying, so a $16^{th}$ order Chebyshev polynomial is not adequate to accurately interpolate the integrand and provide an accurate integration result. Since this subinterval did not converge, this interval will also be bisected. This algorithm is repeated until all subintervals converge to the specified tolerance.

When the adaptive algorithm is complete, the greatest density of abscissas are located near $k_y = k$. Since the nature of the integrand changes after $k_y = k$ to a smooth function, the number of abscissa required may be saved by forcing the adaptive algorithm to execute only on the subinterval $[0, k]$, and integrating $[k, k_c]$ with an integration scheme of sufficient order.

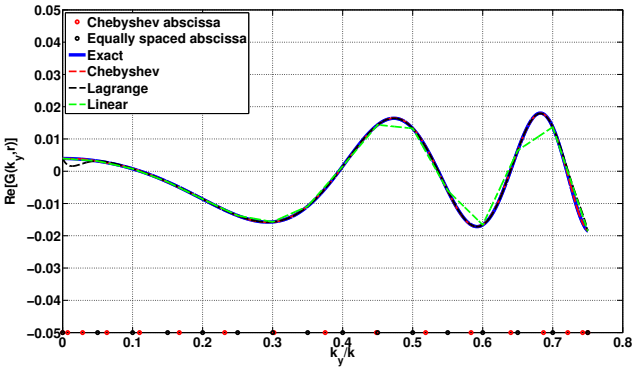


(a)

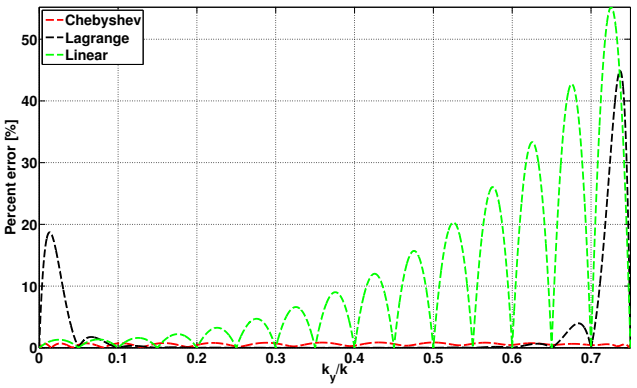


(b)

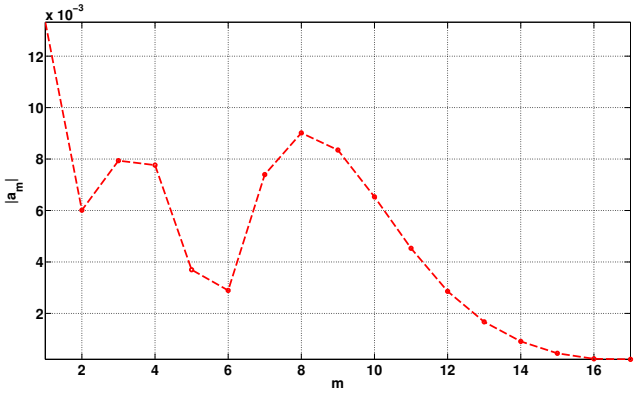


(c)

Figure A.1: (a) Comparison of Chebyshev, Lagrange, and linear interpolation with the exact function for the interval 0 to $k_c/2$. (b) Percent error for Chebyshev, Lagrange, and linear interpolation. (c) Magnitude of the Chebyshev coefficients.

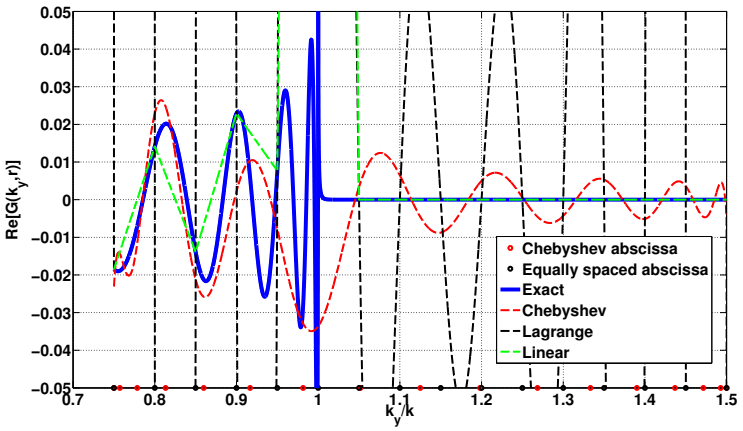


(a)

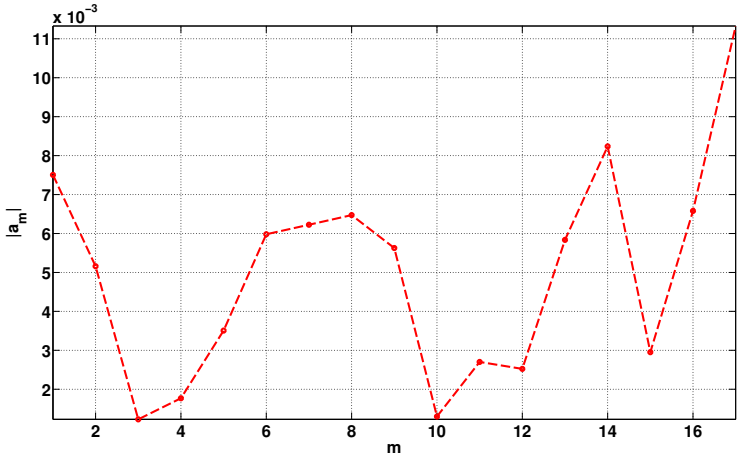


(b)

Figure A.2: (a) Comparison of Chebyshev, Lagrange, and linear interpolation with the exact function for the interval $k_c/2$ to $k_c$. (a) Magnitude of the Chebyshev coefficients.

# Bibliography

[1] A. Tolstoy, K. Smith, and N. Maltsev, "The SWAM'99 workshop-an overview," *Journal of Computational Acoustics*, vol. 9, no. 01, pp. 1–16, 2001.

[2] D. Weston, "Horizontal refraction in a three-dimensional medium of variable stratification," *Proceedings of the Physical Society*, vol. 78, no. 1, p. 46, 1961.

[3] R. Doolittle, A. Tolstoy, and M. Buckingham, "Experimental confirmation of horizontal refraction of CW acoustic radiation from a point source in a wedge-shaped ocean environment," *J. Acoust. Soc. Am.*, vol. 83, no. 6, pp. 2117–2125, 1988.

[4] D. Weston, "Guided propagation in a slowly varying medium," *Proceedings of the Physical Society*, vol. 73, no. 3, p. 365, 1959.

[5] A. D. Pierce, "Extension of the method of normal modes to sound propagation in an almost-stratified medium," *J. Acoust. Soc. Am.*, vol. 37, no. 1, pp. 19–27, 1965.

[6] R. D. Graves, A. Nagl, H. Überall, and G. L. Zarur, "Range dependent normal modes in underwater sound propagation: Application to the

wedgeshaped ocean," *J. Acoust. Soc. Am.*, vol. 58, no. 6, pp. 1171–1177, 1975.

[7] S. R. Rutherford and K. E. Hawker, "Consistent coupled mode theory of sound propagation for a class of nonseparable problems," *J. Acoust. Soc. Am.*, vol. 70, no. 2, pp. 554–564, 1981.

[8] H. Weinberg and R. Burridge, "Horizontal ray theory for ocean acoustics," *J. Acoust. Soc. Am.*, vol. 55, no. 1, pp. 63–79, 1974.

[9] C. H. Harrison, "Acoustic shadow zones in the horizontal plane," *J. Acoust. Soc. Am.*, vol. 65, no. 1, pp. 56–61, 1979.

[10] E. K. Westwood, "Broadband modeling of the three-dimensional penetrable wedge," *J. Acoust. Soc. Am.*, vol. 92, no. 4, pp. 2212–2222, 1992.

[11] R. B. Evans, "A coupled mode solution for acoustic propagation in a waveguide with stepwise depth variations of a penetrable bottom," *J. Acoust. Soc. Am.*, vol. 74, no. 1, pp. 188–195, 1983.

[12] J. M. Arnold and L. B. Felsen, "Rays and local modes in a wedge-shaped ocean," *J. Acoust. Soc. Am.*, vol. 73, no. 4, pp. 1105–1119, 1983.

[13] A. D. Pierce, "Guided mode disappearance during upslope propagation in variable depth shallow water overlying a fluid bottom," *J. Acoust. Soc. Am.*, vol. 72, no. 2, pp. 523–531, 1982.

[14] M. J. Buckingham, "Theory of three-dimensional acoustic propagation in a wedgelike ocean with a penetrable bottom," *J. Acoust. Soc. Am.*, vol. 82, no. 1, pp. 198–210, 1987.

[15] J. M. Arnold and L. B. Felsen, "Intrinsic modes in a nonseparable ocean waveguide," *J. Acoust. Soc. Am.*, vol. 76, no. 3, pp. 850–860, 1984.

[16] Y. Desaubies and K. Dysthe, "Normal-mode propagation in slowly varying ocean waveguides," *J. Acoust. Soc. Am.*, vol. 97, no. 2, pp. 933–946, 1995.

[17] R. Hardin and F. Tappert, "Applications of the split-step Fourier method to the numerical solution of nonlinear and variable coefficient wave equations," *Siam Rev*, vol. 15, no. 2, p. 423, 1973.

[18] F. Tappert, "The parabolic approximation method," in *Wave Propagation and Underwater Acoustics* (J. Keller and J. Papadakis, eds.), vol. 70 of *Lecture Notes in Physics*, pp. 224–287, Springer Berlin Heidelberg, 1977.

[19] F. B. Jensen, W. A. Kuperman, M. B. Porter, and H. Schmidt, *Computational ocean acoustics*. New York: Springer, 2000.

[20] S. T. McDaniel, "Propagation of normal mode in the parabolic approximation," *J. Acoust. Soc. Am.*, vol. 57, no. 2, pp. 307–311, 1975.

[21] J. Claerbout, *Fundamentals of Geophysical Data Processing*. Oxford, UK: Blackwell, 1994.

[22] R. R. Greene, "The rational approximation to the acoustic wave equation with bottom interaction," *J. Acoust. Soc. Am.*, vol. 76, no. 6, pp. 1764–1773, 1984.

[23] L. Halpern and L. N. Trefethen, "Wide-angle one-way wave equations," *J. Acoust. Soc. Am.*, vol. 84, no. 4, pp. 1397–1404, 1988.

[24] A. Bamberger, B. Engquist, L. Halpern, and P. Joly, "Higher order paraxial wave equation approximations in heterogeneous media," *SIAM Journal on Applied Mathematics*, vol. 48, no. 1, pp. 129–154, 1988.

[25] M. D. Collins, "Applications and time-domain solution of higher-order parabolic equations in underwater acoustics," *J. Acoust. Soc. Am.*, vol. 86, no. 3, pp. 1097–1102, 1989.

[26] D. Lee, G. Botseas, and W. L. Siegmann, "Examination of three-dimensional effects using a propagation model with azimuth-coupling capability (FOR3D)," *J. Acoust. Soc. Am.*, vol. 91, no. 6, pp. 3192–3202, 1992.

[27] M. D. Collins, "The adiabatic mode parabolic equation," *J. Acoust. Soc. Am.*, vol. 94, no. 4, pp. 2269–2278, 1993.

[28] A. T. Abawi, W. A. Kuperman, and M. D. Collins, "The coupled mode parabolic equation," *J. Acoust. Soc. Am.*, vol. 102, no. 1, pp. 233–238, 1997.

[29] F. B. Jensen and W. A. Kuperman, "Sound propagation in a wedge-shaped ocean with a penetrable bottom," *J. Acoust. Soc. Am.*, vol. 67, no. 5, pp. 1564–1566, 1980.

[30] G. B. Deane and M. J. Buckingham, "Two approximate solutions for the 3-D field in the ASA benchmark wedge," *J. Acoust. Soc. Am.*, vol. 109, no. 5, pp. 2332–2332, 2001.

[31] C. T. Tindle and Z. Y. Zhang, "An adiabatic normal mode solution for the benchmark wedge," *J. Acoust. Soc. Am.*, vol. 101, no. 1, pp. 606–609, 1997.

[32] G. B. Deane and M. J. Buckingham, "An analysis of the three-dimensional sound field in a penetrable wedge with a stratified fluid or elastic basement," *J. Acoust. Soc. Am.*, vol. 93, no. 3, pp. 1319–1328, 1993.

[33] F. B. Jensen and C. M. Ferla, "Numerical solutions of range-dependent benchmark problems in ocean acoustics," *J. Acoust. Soc. Am.*, vol. 87, no. 4, pp. 1499–1510, 1990.

[34] F. Sturm, "Numerical study of broadband sound pulse propagation in three-dimensional oceanic waveguides," *J. Acoust. Soc. Am.*, vol. 117, no. 3, pp. 1058–1079, 2005.

[35] K. D. Heaney, W. A. Kuperman, and B. E. McDonald, "Perth-Bermuda sound propagation (1960): Adiabatic mode interpretation," *J. Acoust. Soc. Am.*, vol. 90, no. 5, pp. 2586–2594, 1991.

[36] K. D. Heaney and J. J. Murray, "Measurements of three-dimensional propagation in a continental shelf environment," *J. Acoust. Soc. Am.*, vol. 125, no. 3, pp. 1394–1402, 2009.

[37] M. S. Ballard, "Modeling three-dimensional propagation in a continental shelf environment," *J. Acoust. Soc. Am.*, vol. 131, no. 3, pp. 1969–1977, 2012.

[38] K. D. Heaney, R. L. Campbell, and M. Snellen, "Long range acoustic measurements of an undersea volcano," *J. Acoust. Soc. Am.*, vol. 134, no. 4, pp. 3299–3306, 2013.

[39] R. K. Eby, A. O. Williams, R. P. Ryan, and P. Tamarkin, "Study of acoustic propagation in a two-layered model," *J. Acoust. Soc. Am.*, vol. 32, no. 1, pp. 88–99, 1960.

[40] F. Ingenito and S. N. Wolf, "Acoustic propagation in shallow water overlying a consolidated bottom," *J. Acoust. Soc. Am.*, vol. 60, no. 3, pp. 611–617, 1976.

[41] C. T. Tindle, H. Hobaek, and T. G. Muir, "Normal mode filtering for downslope propagation in a shallow water wedge," *J. Acoust. Soc. Am.*, vol. 81, no. 2, pp. 287–294, 1987.

[42] C. T. Tindle and G. B. Deane, "Sound propagation over a sloping bottom using rays with beam displacement," *J. Acoust. Soc. Am.*, vol. 78, no. 4, pp. 1366–1374, 1985.

[43] F. B. Jensen and C. T. Tindle, "Numerical modeling results for mode propagation in a wedge," *J. Acoust. Soc. Am.*, vol. 82, no. 1, pp. 211–216, 1987.

[44] J. N. Reddy, *An Introduction to the Finite Element Method, Third Edition*. New York: McGraw Hill, 2006.

[45] F. Ihlenburg, *Finite Element Analysis of Acoustic Scattering*. New York: Springer, 1998.

[46] E. B. Becker, G. F. Carey, and J. T. Oden, *Finite Elements: An Introduction, Volume I*. New Jersey: Prentice-Hall, 1981.

[47] M. Zampolli, A. Tesei, F. B. Jensen, N. Malm, and J. B. Blottman III, "A computationally efficient finite element model with perfectly matched layers applied to scattering from axially symmetric objects," *J. Acoust. Soc. Am.*, vol. 122, no. 3, pp. 1472–1485, 2007.

[48] M. J. Isakson and N. P. Chotiros, "Finite element modeling of reverberation and transmission loss in shallow water waveguides with rough boundaries," *J. Acoust. Soc. Am.*, vol. 129, no. 3, pp. 1273–1279, 2011.

[49] M. J. Isakson and N. P. Chotiros, "A finite element model of propagation on the southern and western australian continental shelf," in *OCEANS 2010 IEEE-Sydney*, pp. 1–4, IEEE, 2010.

[50] R. J. Darrell and M. D. Richardson, *High-Frequency Seafloor Acoustics*. New York: Springer, 2007.

[51] J. Yang, D. Tang, and E. Thorsos, "Reverberation due to bottom roughness using first-order perturbation theory," in *Proceedings of the International Symposium on Underwater Reverberation and Clutter*, pp. 81–88, 2008.

[52] COMSOL AB, *COMSOL v4.3b Acoustics Module: User's Guide*, May 2013.

[53] J.-P. Bérenger, *Perfectly Matched Layer (PML) for Computational Electromagnetics*. Arcueil, France: Morgan & Claypool, 2007.

[54] B. Zhou and S. Greenhalgh, "An adaptive wavenumber sampling strategy for 2.5-D seismic-wave modeling in the frequency domain," *pure and applied geophysics*, vol. 163, no. 7, pp. 1399–1416, 2006.

[55] B. Zhou, S. Greenhalgh, and M. Greenhalgh, "Wavenumber sampling strategies for 2.5-D frequency-domain seismic wave modelling in general anisotropic media," *Geophysical Journal International*, vol. 188, no. 1, pp. 223–238, 2012.

[56] G. Evans and J. Webster, "A comparison of some methods for the evaluation of highly oscillatory integrals," *Journal of Computational and Applied Mathematics*, vol. 112, no. 1, pp. 55–69, 1999.

[57] H. O'hara and F. J. Smith, "The evaluation of definite integrals by interval subdivision," *The Computer Journal*, vol. 12, no. 2, pp. 179–182, 1969.

[58] M. V. Wilkes, *A Short Introduction to Numerical Analysis*. CUP Archive, 1966.

[59] C. W. Clenshaw and A. R. Curtis, "A method for numerical integration on an automatic computer," *Numerische Mathematik*, vol. 2, no. 1, pp. 197–205, 1960.

[60] D. Elliott, "Truncation errors in two Chebyshev series approximations," *Mathematics of Computation*, vol. 19, no. 90, pp. 234–248, 1965.

[61] H. O'hara and F. J. Smith, "Error estimation in the Clenshaw–Curtis quadrature formula," *The Computer Journal*, vol. 11, no. 2, pp. 213–219, 1968.

[62] I. H. Sloan and W. Smith, "Product-integration with the Clenshaw-Curtis and related points," *Numerische Mathematik*, vol. 30, no. 4, pp. 415–428, 1978.

[63] M. Abramowitz and I. A. Stegun, *Handbook of mathematical functions: with formulas, graphs, and mathematical tables*. Courier Dover Publications, 2012.

[64] D. Elliott, "The evaluation and estimation of the coefficients in the Chebyshev series expansion of a function," *Mathematics of Computation*, vol. 18, no. 86, pp. 274–284, 1964.

[65] D. Nkemzi and W. Green, "Transient wave propagation in a viscoelastic sandwich plate," *Acta mechanica*, vol. 102, no. 1-4, pp. 167–182, 1994.

[66] R. Piessens and M. Branders, "Computation of Fourier transform integrals using Chebyshev series expansions," *Computing*, vol. 32, no. 2, pp. 177–186, 1984.

[67] P.-C. Xu and A. Mal, "An adaptive integration scheme for irregularly oscillatory functions," *Wave Motion*, vol. 7, no. 3, pp. 235–243, 1985.

[68] R. Piessens and M. Branders, "Numerical solution of integral equations of mathematical physics, using Chebyshev polynomials," *Journal of Computational Physics*, vol. 21, no. 2, pp. 178–196, 1976.

[69] J. Oliver, "The numerical solution of linear recurrence relations," *Numerische Mathematik*, vol. 11, no. 4, pp. 349–360, 1968.

[70] L. F. Shampine, "Vectorized adaptive quadrature in matlab," *Journal of Computational and Applied Mathematics*, vol. 211, no. 2, pp. 131–140, 2008.

[71] H. Schmidt, *OASES Version 3.1: User Guide and Reference Manual*. Department of Ocean Engineering, Massachusetts Institute of Technology, March 2011.

[72] M. D. Collins, *User's Guide for RAM Versions 1.0 and 1.0p*. Naval Research Laboratory, Washington, DC, 1995.

[73] J. I. Arvelo and A. P. Rosenberg, "Three-dimensional effects on sound propagation and matched-field processor performance," *J. Comput. Acoust.*, vol. 9, no. 01, pp. 17–39, 2001.

[74] G. H. Brooke, D. J. Thomson, and G. R. Ebbeson, "PECan: A Canadian parabolic equation model for underwater sound propagation," *J. Comput. Acoust.*, vol. 9, no. 01, pp. 69–100, 2001.

[75] A. Gil, J. Segura, and N. M. Temme, *Numerical methods for special functions*. Siam, 2007.

[76] M. A. Biot and I. Tolstoy, "Formulation of wave propagation in infinite media by normal coordinates with an application to diffraction," *J. Acoust. Soc. Am.*, vol. 29, no. 3, pp. 381–391, 1957.

[77] H. Medwin, "Shadowing by finite noise barriers," *J. Acoust. Soc. Am.*, vol. 69, no. 4, pp. 1060–1064, 1981.

[78] K. D. Heaney, R. L. Campbell, and M. Snellen, "Long range acoustic measurements of an undersea volcano," *J. Acoust. Soc. Am.*, vol. 134, no. 4, pp. 3299–3306, 2013.

[79] B. Zhou and S. A. Greenhalgh, "Composite boundary-valued solution of the 2.5-D green's function for arbitrary acoustic media," *Geophysics*, vol. 63, no. 5, pp. 1813–1823, 1998.

# Vita

Benjamin Michael Goldsberry is originally from Jacksonville, Florida. He attended Florida State University for his undergraduate studies, where he graduated Summa Cum Laude with bachelor's degrees in both Applied and Computational Mathematics and Commercial Music in 2012. That summer, Benjamin participated in an internship at NASA Ames Research Center. Benjamin is now a graduate student at The University of Texas at Austin, where he completed a Master's of Science in Mechanical Engineering in 2014. He also holds a graduate research assistantship at the Applied Research Laboratories, performing research in underwater acoustics.

Permanent address: bmgoldsberry@gmail.com

This thesis was typeset with LaTeX[†] by the author.

[†]LaTeX is a document preparation system developed by Leslie Lamport as a special version of Donald Knuth's TeX Program.